


Spring 6-30-2022

Sol-gel Synthesis and Spectroscopic Characterization of Titanium Dioxide Doped with Copper and Iron

Erin L. Jacoski
Skidmore College, ejacoski@skidmore.edu

Follow this and additional works at: https://creativematter.skidmore.edu/chem_stu_schol

 Part of the [Environmental Chemistry Commons](#), [Inorganic Chemistry Commons](#), [Materials Chemistry Commons](#), and the [Other Chemistry Commons](#)

Recommended Citation

Jacoski, Erin L., "Sol-gel Synthesis and Spectroscopic Characterization of Titanium Dioxide Doped with Copper and Iron" (2022). *Chemistry Senior Theses*. 15.
https://creativematter.skidmore.edu/chem_stu_schol/15

This Thesis is brought to you for free and open access by the Chemistry at Creative Matter. It has been accepted for inclusion in Chemistry Senior Theses by an authorized administrator of Creative Matter. For more information, please contact dseiler@skidmore.edu.

Sol-gel Synthesis and Spectroscopic
Characterization of Titanium Dioxide
Doped with Copper and Iron

By Erin Jacoski

Senior Thesis, 2022

Skidmore College

ABSTRACT

A source of bioavailable iron in open oceans stems from aerosols, increasing phytoplankton growth and the sequestration of atmospheric carbon dioxide. These aerosols contain semiconductors, like titanium dioxide, which is known to increase the bioavailability and can trigger photoreduction of Fe^{3+} . Recently, it is suspected that other metals in the aerosols also influence the release of iron. In this work, the effects of doping with iron and copper on the physical characteristics of titanium dioxide nanoparticles, since the photocatalytic potential of titanium dioxide depends on its structure and metal content (anatase vs. rutile), were explored. Titanium dioxide nanoparticles were prepared using a sol-gel synthesis with iron, copper, or both metals. These particles were characterized using x-ray diffraction, x-ray fluorescence, scanning electron microscopy, and diffuse reflectance spectroscopy. Overall, the addition of the metal(s) before or after the condensation of titanium affected the crystallinity, metal uptake, and band gap energy and wavelength of the doped semiconductor. Co-doping after titanium was added produced porous semiconductor particles with more iron and copper incorporated, a smaller conversion into rutile structure, the smallest band gap, and the largest wavelength. These doped particles will be further used to better understand the mechanism of how iron becomes bioavailable in the atmosphere.

TABLE OF CONTENTS

ABSTRACT.....	2
LIST OF FIGURES	6
LIST OF TABLES	8
Chapter 1. INTRODUCTION.....	9
1.1 Motivation.....	9
1.2 Environmental relevance of TiO ₂ photocatalysis	9
1.3 Semiconductors and photocatalysis	10
1.4 Synthesis of titanium dioxide doped with metals	12
1.5 Experimental Aims	14
1.6 Characterization of crystal structure via XRD.....	15
1.7 Characterization via metal composition via XRF.....	17
1.8 Characterization of morphology via SEM.....	17
1.9 Characterization of band gap via DRS	18
Chapter 2. EXPERIMENTAL WORK.....	20
2.1 Reagents.....	20
2.2 Syntheses	20
2.2.1 Synthesis of Titanium + Metals.....	20
2.2.3 Synthesis of Metals + Titanium.....	21
2.2.4 TiO ₂ control.	22
2.2.5 Reagents control.	22

2.3 Characterization techniques	22
2.3.1 X-Ray Diffraction.	22
2.3.2 X-Ray Fluorescence.....	24
2.3.3 Scanning Electron Microscopy.....	24
2.3.4 Diffuse Reflectance Spectroscopy.....	24
Chapter 3. RESULTS.....	26
3.1 TiO ₂ co-doped with copper and iron	26
3.1.1 X-ray diffraction of co-doped TiO ₂	26
3.1.2 X-ray fluorescence of co-doped TiO ₂	32
3.1.3 Scanning electron microscopy of co-doped TiO ₂	34
3.1.4 Diffuse reflectance spectroscopy of co-doped TiO ₂	34
3.2 TiO ₂ doped with copper.....	38
3.2.1 X-ray diffraction of copper doped TiO ₂	38
3.2.2 X-ray fluorescence of copper doped TiO ₂	40
3.2.3 Scanning electron microscopy of copper doped TiO ₂	40
3.2.4 Diffuse reflectance spectroscopy of copper doped TiO ₂	40
3.3 TiO ₂ doped with iron	44
3.3.1 X-ray diffraction of iron doped TiO ₂	44
3.3.2 X-ray fluorescence of iron doped TiO ₂	46
3.3.3 Scanning electron microscopy of iron doped TiO ₂	46

3.3.4 Diffuse reflectance spectroscopy of iron doped TiO ₂	46
Chapter 4. DISCUSSION	51
4.1 X-ray diffraction	51
4.2 X-ray fluorescence.....	53
4.3 Scanning electron microscopy	55
4.4. Diffusion reflectance spectroscopy.....	56
Chapter 5. CONCLUSIONS	60
ACKNOWLEDGEMENTS	62
REFERENCES	63
TERMS AND ABBREVIATIONS	67
APPENDEXIS	68
Appendix 1. Reference data for XRD.....	68
Appendix 2. Example of calculation of crystallinity parameters	69
Grain Size	69
Lattice parameters.....	70
Appendix 3. Calculation of Anatase and Rutile proportions from XRD data	72
Appendix 4. Calculation of band gap from DRS Kubelka-Munk function and Tauc plot method.....	73
Appendix 5. XRF data	74
Appendix 6. Proportion of Fe:Cu in co-doped products.....	75

LIST OF FIGURES

Figure 1.1. Crystal structures of anatase, rutile, and brookite [Katal 2020]	11
Figure 1.2. Scheme of the synthesis of TiO ₂ via sol-gel method. [Guzmán-Velderrain 2014] ...	13
Figure 1.3. Tetragonal lattice structure where lengths $a = b \neq c$	16
Figure 2.1. Experimental approach. Left shows the synthesis of doped TiO ₂ when titanium (IV) isopropoxide is reacted before adding doping metal. Right shows the synthesis of doped TiO ₂ when doping metal are reacted before adding titanium (IV) isopropoxide.	21
Figure 3.1. Offset XRD spectra of co-doped products, titanium dioxide control and calcined reagents. The main peak in each spectrum represents 100% intensity.	27
Figure 3.2. (left) Offset diffraction patterns of synthesized TiO ₂ and reference anatase and rutile. (Right) Offset diffraction patterns of calcined reagents and reference anatase and rutile.....	29
Figure 3.3. (left) Offset diffraction patterns of Ti + M co-doped product (added metals after the titanium) and reference anatase and rutile. (Right) Offset diffraction patterns of M + Ti co-doped product (added metals before the titanium) and reference anatase and rutile.....	30
Figure 3.4. XRF spectra of calcined reagents (yellow), titanium dioxide control (black), and co-doped products from Ti + M (red) and M + Ti (blue). Peaks attributed to titanium are at 4.499 and 4.921 keV, iron are at 6.407 and 7.070 keV, and copper are at 8.034 and 8.918 keV.....	33
Figure 3.5. SEM images of (A) titanium dioxide control, (B) calcined reagents, (C) Ti+M co-doped product, and (D) M+Ti co-doped product. Scale bar apply to all micrographs.	35
Figure 3.6. (Left) DRS spectra with photograph, and (right) corresponding Tauc plots showing extrapolation and linear regression equation for (top) commercial TiO ₂ , (middle) titanium dioxide control, and (bottom) calcined reagents. All were measured with R ² values greater the 0.99.....	36
Figure 3.7. (Left) DRS spectra with photograph, and (right) corresponding Tauc plots showing extrapolation and linear regression for co-doped product (top) Ti + M and (bottom) M+ Ti. All were measured with R ² values greater than 0.99.	37
Figure 3.8. (left) Offset diffraction patterns of doped product from Ti + Cu synthesis (adding metals after titanium has been reacted) and reference anatase and rutile. (Right) Offset diffraction patterns of doped product from Cu + Ti synthesis (adding metals and titanium together) and reference anatase and rutile.....	39

Figure 3.9. XRF spectra of calcined reagents (yellow), titanium dioxide control (black), and doped products from Ti + Cu (red) and Cu + Ti (blue). Peaks attributed to titanium are at 4.499 and 4.921 keV, iron are at 6.407 and 7.070 keV, and copper are at 8.034 and 8.918 keV..... 41

Figure 3.10. SEM images of (A) titanium dioxide control, (B) calcined reagents, (C) Ti + Cu, and (D) Cu + Ti doped product. Scale bar apply to all micrographs. 42

Figure 3.11. (Left) DRS spectra with photograph and (right) corresponding Tauc plots showing extrapolation and linear regression equation for doped product (top) Ti + Cu and (bottom) Cu + Ti. All were measured with R^2 values greater than 0.99. 43

Figure 3.12. (left) Offset diffraction patterns of doped product from Ti + Fe synthesis (adding metals after titanium has been reacted) and reference anatase and rutile. (Right) Offset diffraction patterns of doped product from Fe + Ti synthesis (adding metals and titanium together) and reference anatase and rutile..... 45

Figure 3.13. XRF spectra of calcined reagents (yellow), titanium dioxide control (black), and doped products from Ti + Fe (red) and Fe + Ti (blue). Peaks attributed to titanium are at 4.499 and 4.921 keV, iron are at 6.407 and 7.070 keV, and copper are at 8.034 and 8.918 keV..... 47

Figure 3.14. SEM images of (A) titanium dioxide control, (B) calcined reagents, (C) Ti + Fe, and (D) Fe + Ti doped products. Scale bar apply to all micrographs. 48

Figure 3.15. (Left) DRS spectra with photograph, and (right) corresponding Tauc plots showing extrapolation and linear regression for (top) Ti + Fe and (bottom) Fe + Ti doped products. All measured were with R^2 values greater than 0.99. 49

LIST OF TABLES

Table 3.1. Anatase's lattice parameters and grain size for titanium oxide control, calcined reagents, and co-doped products.....	30
Table 3.2. Percent of anatase and rutile in titanium dioxide control and co-doped products calculated from the main diffraction peak (facets shown in parenthesis).....	32
Table 3.3. Intensity of titanium, iron, and copper at K energy levels for the titanium dioxide control, calcined reagents, and co-doped products. Noise = 29 intensity units. Full XRF data in Appendix 5.....	33
Table 3.4. Summary of band gap wavelength and energy for reagents and co-doped products..	37
Table 3.5. Anatase's lattice parameters and grain size for TiO ₂ , calcined reagents, and copper doped TiO ₂	39
Table 3.6. Intensity of titanium, iron, and copper at K energy levels for the titanium dioxide control, calcined reagents, and copper doped products. Noise = 29 intensity units. Full XRF data in Appendix 5.....	41
Table 3.7. Summary of wavelength and band gap energy for reagents and copper doped products.....	43
Table 3.8. Anatase's lattice parameters and grain size for TiO ₂ , calcined reagents, and iron doped TiO ₂	45
Table 3.9. Intensity of titanium, iron, and copper at K energy levels for the titanium dioxide control, calcined reagents, and iron doped products. Noise = 29 intensity units. Full XRF data in Appendix 5.....	47
Table 3.10. Summary of wavelength and band gap energy for reagents and iron doped products.	49
Table 3.11. Comparison of results by technique.....	50

Chapter 1. INTRODUCTION

1.1 Motivation

Titanium dioxide (TiO_2) is considered one of the most promising semiconductors used as a photocatalyst for processes such as water-splitting, solar cells, hydrogen generation, and air, water, and wastewater treatment. The material is favored because it costs very little, is non-toxic, has chemical and photo stability, and has high photocatalytic activity [Katal 2020, Rahimi 2016]. When TiO_2 is a part of aerosol particles, the photocatalytic activity of TiO_2 has direct and indirect effects on the chemical balance of the atmosphere. One of the indirect photocatalytic mechanisms of TiO_2 is presumed to involve iron and copper [Kim 2020]. Before such a mechanism can be elucidated, controlling and understanding of the semiconductor characteristics needs to be assessed. In this work, the effects of the synthesis on TiO_2 structure and photocatalytic properties are studied. There is a focus on the steps in which iron and copper are incorporated in the synthesis.

1.2 Environmental relevance of TiO_2 photocatalysis

The photocatalytic activity is important when looking at TiO_2 in aerosols. Titanium dioxide is a common trace metal oxide in particulate matter, primarily from mineral dust, but also ash from coal-fired power plants [Ostaszewski 2018]. Fly ash, the combustion particles emitted from coal-fired plants, and mineral dust also commonly contain iron oxides and can contain copper oxides [Kim 2020]. The reduced iron, Fe^{2+} , acts as a source of bioavailable iron in open oceans, prompting phytoplankton growth and the sequestration of atmospheric CO_2 [Borgatta 2016].

Titanium dioxide can aid in the reduction process by acting as a reducing agent with the photoexcited electrons [Landi 2022]. The excited electrons in the conduction band can trigger other reduction reactions used to photoreduce Fe^{3+} within the particle, allowing Fe^{2+} to become bioavailable. It is hypothesized that the addition of iron and copper into the crystal of the titanium dioxide will increase the photocatalytic activity and in turn, aid in reduction reactions of iron in the particulate matter [Kim 2020]. This paper will analyze the addition of iron and copper in titanium dioxide and determine the photocatalytic effects of them being added together, separately, and in different addition orders to explore this hypothesis.

1.3 Semiconductors and photocatalysis

Semiconductors can capture energy and transfer it to catalyze chemical reactions. The ability for a semiconductor to act as a good photocatalyst is dependent on the energy gap between the top of the valence band and the bottom of the conduction band, known as the band gap [Landi 2022]. Energy at an appropriate wavelength will excite electrons in the valence band, causing them to overcome the energy barrier, jumping to the conduction band and leaving a hole in the valence band [Yoong 2009]. The excited electrons can quickly release that energy as heat or a photon and fill a hole in the valence band within 10-100 ns [Park 2013]. Alternatively, the electrons act as a good reductant, completing the slower process of charge transfer with another molecule such as oxygen, since they have similar conduction band energy level to reduction potential, in about 0.33 ms [Park 2013, Landi 2022]. This reduction potential could also be used to convert Fe^{3+} to Fe^{2+} .

The energy that is captured and released depends on physical chemical parameters of the semiconductor and environment. Since the rate-determining step of photocatalysis is based on

the rate of charge transfer, the addition of a stronger electron acceptor, like copper and iron that are more electronegative, can increase the photocatalytic rate [Park 2013].

Titanium dioxide has 3 primary crystal structures with three different structures (Figure 1.1): anatase, which is stable at low temperatures, rutile, which is stable at high temperatures, and brookite, that is found in minerals [Rahimi 2016, Katal 2020]. The structures have different types of band gaps. Rutile and brookite have direct band gaps, where the minimum of the conduction band and maximum of the valance band align. Anatase has an indirect band gap where the bands do not perfectly align. [Lance 2018]. Anatase is the most photoactive due to the number of hydroxyl groups, having the largest band gap of 3.2 eV, a larger surface area, and greater porosity compared to the other structures of titanium dioxide. Whereas the rutile structure has a band gap of 3.0 eV [Thambiliyagodage 2021].

One drawback of titanium dioxide as a photocatalyst is that the band gap is only suited to absorb energy for excitation in the UV at 338 nm or less. This means that titanium dioxide in the

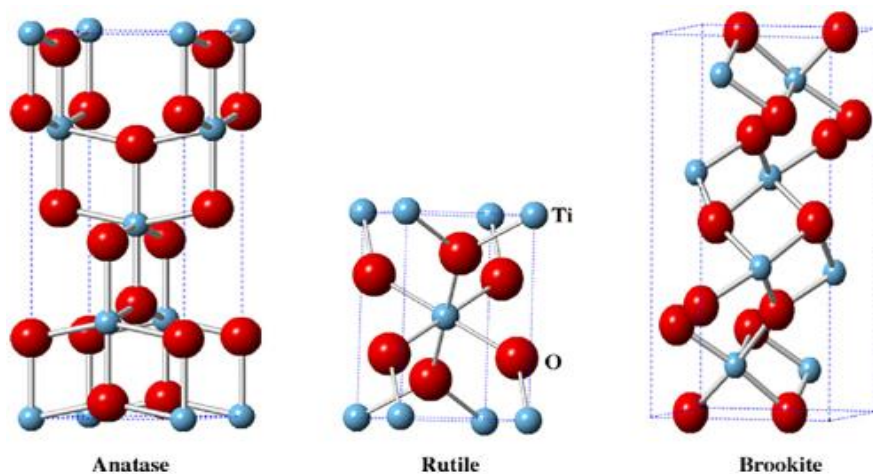


Figure 1.1. Crystal structures of anatase, rutile, and brookite [Katal 2020]

atmosphere is only able to absorb 3-4% of solar radiation [Yoong 2009, Pelaez 2012]. Iron and copper have specific effects on the photocatalytic activity of titanium dioxide. Additionally, doping with metals can slow electron-hole recombination and lessen the band gap, shifting the absorption wavelength [Yoong 2009]. By doping titanium dioxide with metals, such as iron and copper, the band gap would shift to absorb larger wavelengths in the visible region, allowing the particles absorb more solar radiation, and decrease the rate of electron-hole recombination [Yoong 2009]. The iron III and titanium IV have similar atomic radii of 0.745 Å and 0.785 Å respectively, so the iron dopes via substitution. Copper II is much larger than titanium IV at 0.870 Å, so it dopes via the interstitial position of the lattice [Byrne 2019]. This causes distortion to the lattice and allows for doping to be confirmed by calculating the lattice parameters [Thambiliyagodage 2021].

1.4 Synthesis of titanium dioxide doped with metals

A sol-gel synthesis to form and dope titanium dioxide nanoparticles is one of the most common methods. Sol-gel is considered a bottom-up synthesis, where the sol is the main homogeneous molecules that become 3D and heavy, forming a wet gel [Ullattil 2017, Bokov 2021]. The synthesis consists of the hydrolysis/condensation of titanium alkoxide followed by calcination as shown in Figure 1.2.

A common change in method is the source of the metals. Titanium sources include titanium (IV) isopropoxide, titanium (IV) chloride, tetrabutyl titante, titanium butoxide, or tetrabutixytanium [Ismael 2020, Hu 2020, Lin 2018, Thambiliyagodage 2021, Zhang 2014]. The reaction takes place in an alcohol solvent with an acid, to help dissolve the titanium source before the doping metal is added.

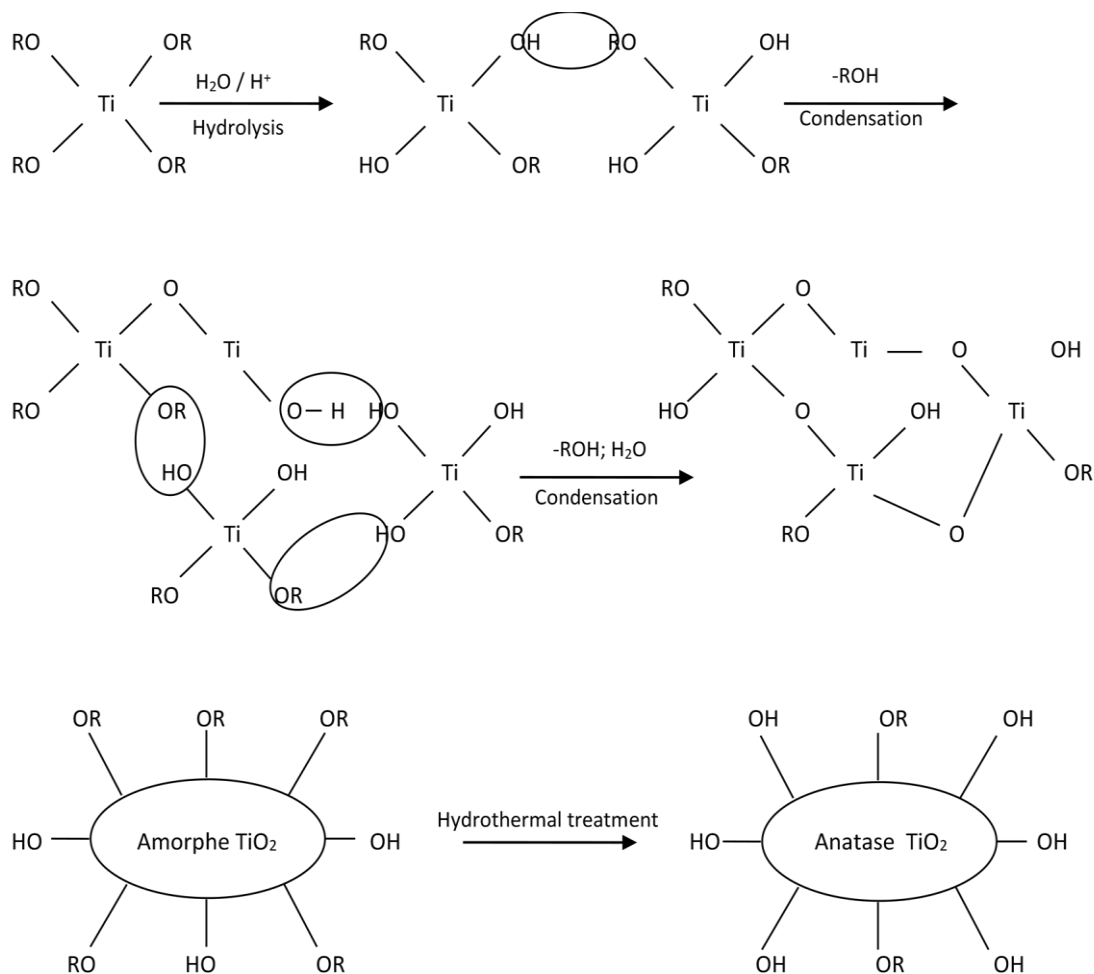


Figure 1.2. Scheme of the synthesis of TiO_2 via sol-gel method. [Guzmán-Velderrain 2014]

Doping with copper is done with copper (II) nitrate or copper (II) hydroxide [Thambiliyagodage 2021, Zhang 2014]. The source for iron doping is iron (II) nitrate [Thambiliyagodage 2021]. Some syntheses include steps such as ultrasonic baths and centrifugation [Ismael 2020, Quyen 2021]. This aids in mixing and the separation of the precipitated particles from the solvent. However, the synthesis from Thambiliyagodage and Mirihana was the only one found that attempted to co-dope with both copper and iron into titanium dioxide nanoparticles, so that was the foundation of the experimental procedure used.

An array of characterizations can be found across the literature, with some being more common than others. X-ray diffraction (XRD) and electron microscopy, sometimes with energy-dispersive x-ray spectroscopy applied (either transition or scanning- TEM or SEM) are almost always used for crystalline structure identification, confirmation of doping, and images of morphology [Ismael 2020, Li 2008, Lin 2018, Oganisian 2015, Quyen 2021, Sohrabi 2016, Thambiliyagodage 2021, Zhang 2014, Zhang 2020]. Other frequent characterization techniques included UV-visible spectroscopy or, more specifically, diffuse reflectance spectroscopy (UV-vis or DRS), X-ray photoelectron spectroscopy (XPS), Raman spectroscopy, x-ray fluorescence (XRF), electrochemical impedance spectroscopy (EIS), and atomic force microscopy (AFM) [Ismael 2020, Lin 2018, Nabi 2008, Quyen 2021, Thambiliyagodage 2021, Zhang 2014, Zhang 2020]. These techniques are used to determine band gaps, analyze the surface chemistry, confirm crystal structures, observe metal distribution, analyze charge transfer, and to establish the magnetic properties per particle, respectively [Ismael 2020, Lin 2018, Nabi 2008, Oganisian 2015, Thambiliyagodage 2021, Zhang 2014, Zhang 2020]. Since the motivation for experimentation is related to band gaps and shift in absorption wavelength, XRD, XRF, SEM, and DRS were used for particle analysis.

1.5 Experimental Aims

As mentioned, the synthesis and characterization procedure for titanium dioxide co-doped with copper and iron was adapted from Thambiliyagodage and Mirihana [Thambiliyagodage 2021]. Experimentation was done to look at the effects of each metal and the order of metal addition had on the doped products. Since Thambiliyagodage and Mirihana were successful in doping when calcined at 450°C, and Yoong et al. found that copper doped titanium dioxide calcined at the lowest temperature of 300°C showed the best photocatalytic activity

experimentation looked at the possibility of co-doping at low temperature of 240°C [Thambiliyagodage 2021, Yoong 2009]. Additionally, the order of when the metals were added was investigated by looking titanium dioxide nanoparticles being formed and then adding the metals (Ti + M), compared to adding the metals in solution before forming the titanium dioxide nanoparticles (M+Ti). To assess the individual effect of the metals, similar syntheses were carried out with the doping of a single metals. Titanium dioxide nanoparticles being formed and then adding copper (Ti + Cu) or iron (Ti + Fe) is compared to titanium dioxide nanoparticles being formed after adding copper (Cu + Ti) or iron (Fe + Ti).

The sol-gel procedure by Thambiliyagodage and Mirihana was followed, changing the order of the metals being added, doping with individual metals, and lowering the calcination temperature to 240°C. Extensive characterization with XRD, XRF, SEM and DRS was completed to determine if the product was doped and the affects that had on the crystal structure and band gap.

1.6 Characterization of crystal structure via XRD

X-rays can interact with the material in ways including absorption, emission, refraction, and diffraction. For samples that are polycrystalline, powder x-ray diffraction becomes the most reliable method to determine each crystal structure. X-ray diffraction works by shooting x-rays at the sample and measuring the scattering that results. For powder diffraction, the scattered intensity is measured as a function of the Bragg angle (2θ). When there are alterations to the lattice, the distances between atoms, the relative intensities and/or the position of the peak changes consequently. This allows for the ratio of each crystalline structure of the polycrystalline sample to be calculated. More microscopic information can also be extracted since a grain size

below a certain limit and strained or deformed materials also affect the peak shape [Pecharsky 2009].

The lattice parameters change as a consequence of doping. By nature, anatase and rutile have tetragonal crystal structures (Figure 1.3) and brookite has a rhombohedral crystal structure. The difference in radii of titanium and iron and introduction of large copper atoms causes distortion to the tetragonal structure when doped. This distortion can be calculated using Bragg's law by calculating the side lengths of the structure. Lattice parameters that differ from that of anatase and rutile are indicative of doping [Thambiliyagodage 2021]. According to the Braggs, the reflection of x-rays with identical Millar indices occurs in a series of equally spaced parallel planes at a specific angle(s). This results in a path difference, which requires the interplanar distance, d , to be calculated before determining the lattice parameters [Pecharsky 2009].

To calculate d and grain size the wavelength of the generated x-rays is needed, making knowledge of the anode that generates the x-rays the most important instrumental parameter. Other instrumental parameters that can be changed are the voltage, current, the range of Bragg angle measurements and the step and speed of those angles. The voltage and current changes the intensity of the x-ray beam, therefore affecting the intensity of each peak. The step and speed of

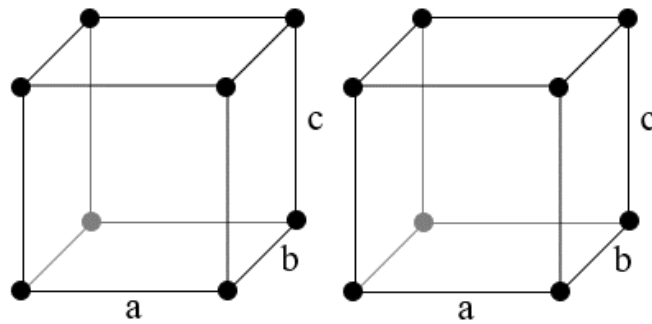


Figure 1.3. Tetragonal lattice structure where lengths $a = b \neq c$.

the measuring angles affects the time it takes to run a sample and the resolution of spectra. For our experimentation, x-ray diffraction was used to determine if the product was doped based on the lattice parameter calculations, the crystal structure of the products with the relative percentages, and the average grain size of the nanoparticles.

1.7 Characterization via metal composition via XRF

Due to the large energy of incoming x-rays, absorption into the material can enhance oscillations of the lattice or cause the emission of photoelectrons by exciting the atoms. The signal comes from an electron from the inner shells of the atom or, if the atom is excited, relaxation back to the ground state completed by emitting electromagnetic radiation. The emission from each atom is specific to the element, allowing for elemental analysis to take place. This allows x-ray fluorescence to be used for elemental analysis, looking for evidence of copper and iron in the crystals. While the parameters typically are not changed for the instrument, taking note of the high voltage and anode current can still be necessary. Additionally, filters can be added to block certain atom signals for elemental analysis of an element that may overlap. For more detailed information about XRF theory and instrumentation see the review by Haschke [Haschke 2014].

1.8 Characterization of morphology via SEM

Scanning electron microscopy was used to look at the surface of the particles and assess the porosity. The SEM uses a focused x-ray electron beam to scan across the surface of the material. The absorption of the x-rays causes elastic and inelastic interactions, and the emission of x-rays, Auger electrons, and cathodoluminescence. The image is formed as a result of elastic and inelastic interactions. Elastic scattering occurs by deflecting the beam by a nucleus or outer shell

electrons with similar energy in the material, causing relatively no energy loss, but a wide-angle directional change. Any elastically scattered electron with angles above 90 degrees and with an energy greater than 50 eV are considered backscattered electrons and can be used to determine both compositional and topographic information. Inelastic collisions occur when the incoming x-ray beam transfers substantial energy to the atoms. This leads to the generation of secondary electrons that have energies less than 50 eV and can be used to form an image.

The primary parameter that can be changed is beam accelerating voltage. The volume and depth of penetration of the rays increases with increased beam energy and decreases with increasing sample atomic numbers, since they have most particles to stop electron penetration. The surface resolution of the particles greatly decreases with high accelerating voltage, such as 20 kV or higher. For more detailed information about SEM theory and instrumentation see the review by Zhou and Wang [Zhou 2007].

1.9 Characterization of band gap via DRS

Diffuse reflectance spectroscopy was used to measure the percent reflectance, observe the shift in wavelength absorption, and calculate the band gap from the valance band to the conduction band. When waves of visible and ultra-violet light are targeted at the sample, there is reflection, refraction, diffraction and absorption by the particles in all directions, together these result in diffuse reflection. When the dimensions of the particle are similar to, or smaller than, the wavelength, and the particles are closely packed, multiple scattering occurs. This scattering cannot be separated from refraction, diffraction, and absorption in the spectra due to its changes on intensity and angular distribution of the radiation. A theory used to get past that issue is the Kubelka-Munk theory. This model assumes that the thickness of sample that is responsible for

scattering and absorbing radiation is canceled with a diffuse monochromatic radiation flux as the thickness approaches infinity. Additionally, the system must have cylindrical geometry with a flat area so the boundaries' effects can be voided. Since the thickness of a sample cannot actually be infinite, a thickness of 1 mm or greater is sufficient for calculations using the Kubelka-Munk Function. Use of the Kubelka-Munk function will be further discussed later, however, to estimate the band gap, use of Tauc plots is also required. Combining these methods allowed for the band gap energy and band gap wavelength to be estimated for each sample [Landi 2022].

The main parameters that can be changed include the range of measurements, the wavelength of lamp change, slit width, scan speed, and data intervals. The wavelengths chosen for the range of measurements depend on the wavelength of the expected band gap, so that the band gap wavelength is in the spectra. Change in lamp can cause an artifact in the spectra, making it important to choose a wavelength outside the range of the expected band gap. The slit width, scan speed and data intervals all affect the resolution of the resulting spectra.

Chapter 2. EXPERIMENTAL WORK

2.1 Reagents

All reagents were purchased and used as received. Iron (II, III) oxide black magnetite from STREM chemicals; concentrated nitric acid from J.T. Baker; titanium (IV) dioxide (anatase), iron (III) nitrate nonahydrated, and titanium (IV) isopropoxide from Sigma-Aldrich; ethanol 95% and copper (II) nitrate from Fisher scientific; copper (II) oxide from Alfa Aesar. Deionized 18 MΩ water was obtained using a Barnstead purification system.

2.2 Syntheses

The titanium nanoparticles doped with metals were prepared via sol-gel synthesis. Doping was done by adding copper, iron, or both at different stages of the hydrolysis/condensation step. The syntheses labeled as Ti + M, Ti + Cu, and Ti + Fe correspond to the reaction of titanium (IV) isopropoxide for 2 h before adding doping metal (Figure 2.1 left). The syntheses labeled as M + Ti, Cu + Ti, and Fe + Ti correspond to the reaction of the doping metals for 2 h before adding titanium (IV) isopropoxide (Figure 2.1 right).

2.2.1 Synthesis of Titanium + Metals.

Experimental conditions were adapted from the work by Thambiliyagodage and Mirihana, [Thambiliyagodage 2021]. A solution of 30 mL ethanol, 10 mL titanium isopropoxide, and 10 mL of 50% nitric acid was covered and stirred for 2 hours. Then 170 μL of 0.1M iron (III) nitrate, or copper (II) nitrate, or both, were added to solution and stirred overnight. The

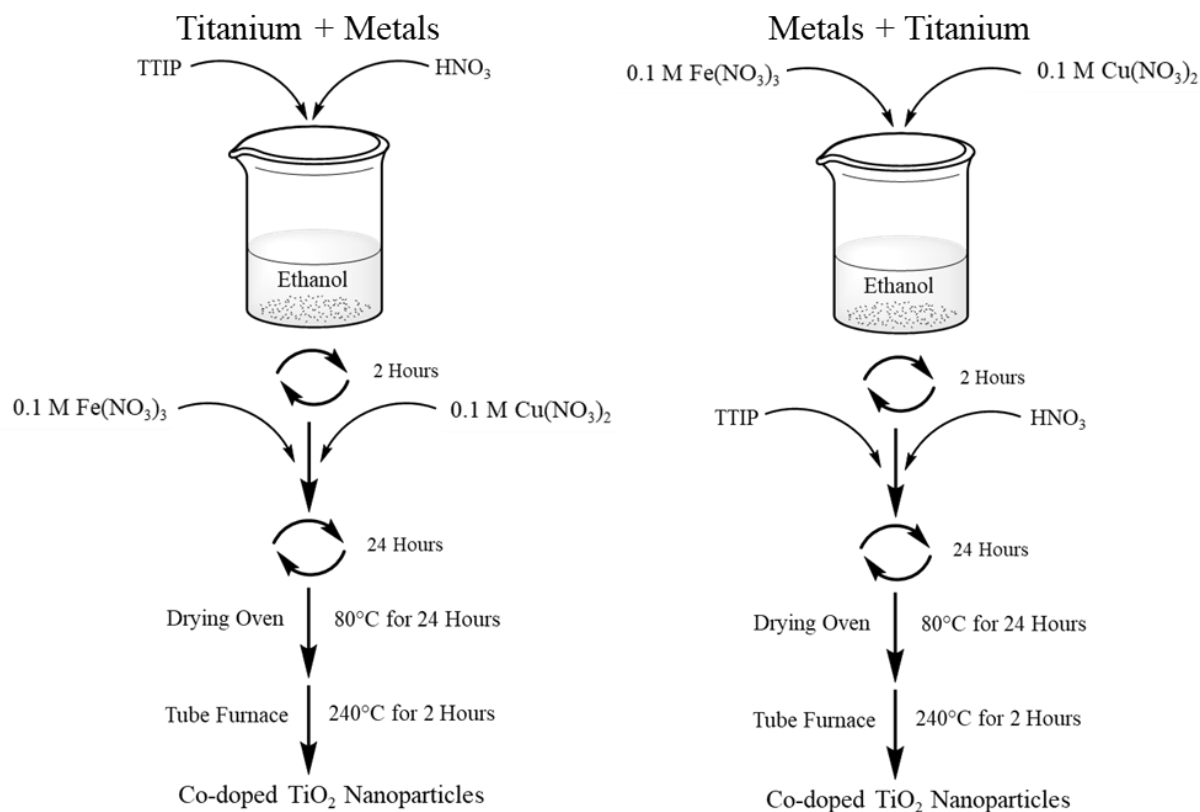


Figure 2.1. Experimental approach. Left shows the synthesis of doped TiO₂ when titanium (IV) isopropoxide is reacted before adding doping metal. Right shows the synthesis of doped TiO₂ when doping metal are reacted before adding titanium (IV) isopropoxide.

remaining ethanol was boiled off while stirring continued. The particles were dried overnight in an 80°C drying oven. The dried product was then calcined at 240°C for 2 hours in a tube furnace.

2.2.3 Synthesis of Metals + Titanium.

Experimental conditions were adapted from the work by Thambiliyagodage and Mirihana, [Thambiliyagodage 2021]. A solution of 30 mL ethanol and 170 μ L of 0.1M iron (III) nitrate, or copper (II) nitrate, or both, was covered and stirred for 2 hours. Then 10 mL of titanium isopropoxide and 10 mL of 50% nitric acid was added and left to stir overnight. The remaining

ethanol was boiled off while continuing to stir. The particles were dried overnight in an 80°C drying oven. The dried product was calcined at 240°C for 2 hours in a tube furnace.

2.2.4 TiO₂ control.

An experimental control titanium dioxide was synthesised adapting the conditions from the work by Thambiliyagodage and Mirihana, [Thambiliyagodage 2021]. A volume of 5 mL of titanium isopropoxide and 10 mL of 50% nitric acid were added to 50 mL of ethanol and was stirred for 2 hours. Then 30 mL of deionized 18 MΩ water was added. The solution continued to stir for 24 hours, then the remaining solvent was boiled off. The powder was left to dry uncovered in a hood overnight. The dried powder was calcined at 500 °C for 2 hours.

2.2.5 Reagents control.

A control mixture of calcined reagents was created by mixing 0.169 moles of titanium (IV) dioxide, with 0.015 moles of copper (II) oxide, and 0.005 moles of iron (II, III) oxide black magnetite. The mixture was dissolved in ethanol and stirred. The ethanol was boiled off. The dried mixture was calcined at 500 °C for 2 hours.

2.3 Characterization techniques

2.3.1 X-Ray Diffraction.

XRD was performed on a Rigaku Miniflex 6G. Measurements were taken at 40 kV and 15 mA. X-rays were generated with a copper anode at a wavelength of 0.15406 nm. Measurements of 2θ ranged from 5° to 80° in 0.02° step at a speed of 2° per minute. Samples were prepared with slight compression into the sample plate.

Identification of TiO₂ crystal structure was done by matching to reference spectra from the International Center for Diffraction Data (JCPDS = Join Committee on Powder Diffraction Standards). Rutile JCPDS no. 88-1175 and Anatase JCPDS no. 84-1286. [Thamaphat, 2010] These values are summarized in Appendix 1.

Before calculating the grain size of the crystals, the full width half max (FWHM) was determined using the originlab pro software. The average crystallite size was calculated for each peak with the respective FWHM using the Scherrer equation (equation 1):

$$\Phi = \frac{K \lambda}{\beta \cos \theta} \quad [1]$$

where Φ is the crystallite size, K is the shape factor, λ is the X-ray wavelength, β is the full line width at the half-maximum height of the main intensity peak and θ is the Bragg angle [Pecharsky 2009]. An average of the sizes and the standard deviation was determined for each sample with peaks that had a FWHM error less than 5. An example calculation can be found in Appendix 2.

Doping was confirmed by calculating the lattice parameters of anatase using Bragg's law with the tetragonal formula (equation 2):

$$\frac{1}{d^2} = \frac{h^2}{a^2} + \frac{k^2}{b^2} + \frac{l^2}{c^2} \quad [2]$$

where d is the distance between adjacent lattice plane, a , b , and c are lattice parameters ($a=b$), and h , k , l are lattice vectors in Millar index notation [Thambiliyagodage 2020]. The distance between adjacent lattice planes (d) was calculated with equation 3, where n is the order of diffraction, that is assumed to be 1 [Pecharsky 2009].

$$d = \frac{n\lambda}{2\sin\theta} \quad [3]$$

The XRD peaks associated with the anatase Miller indices of 101 and 200, at about 25.4° and 48.2°, were used for calculations of lattice parameters in radians. An example calculation can be seen in Appendix 2.

The fraction of rutile was calculated using equation 4 [Spurr 1957]:

$$F_R = \left(1 + 0.8 \left[\frac{I_{A(101)}}{I_{R(110)}} \right] \right)^{-1} \times 100 \quad [4]$$

where F_R is the fraction of rutile in the sample, and $I_{A(101)}$ and $I_{R(110)}$ are the intensities of the main diffraction peaks of anatase and rutile, respectively. An example calculation can be seen in Appendix 3.

2.3.2 X-Ray Fluorescence.

XRF was completed on a Bruker Tracer III SD with a rhodium anode. Measurements were taken at 40 kV and 15 μ A. Samples were measured through a Chemplex Industries SpectroMembrane prolene thin-film. No additional filters were added.

2.3.3 Scanning Electron Microscopy.

SEM was performed on a FEI Quattro S Field Emission Scanning Microscope. The sample was adhered to a stub using carbon stickers. A spot size of 4 was used and a voltage of 10 kV under high vacuum.

2.3.4 Diffuse Reflectance Spectroscopy.

DRS was performed on a PerkinElmer Lambda 35 UV/VIS Spectrometer with a labsphere reflectance spectroscopy accessory. The sample was ground with a mortar and pestle, then compressed and measured through a quartz window. Scans were taken from 200-1100 nm, with a

slit width of 1 nm, scan speed of 480 nm, scanning at every nm. Additionally, there is a lamp change at 532 nm.

The spectra were smoothed using the originlab pro software. The band gap was estimated using the Kubelka-Munk function and Tauc plot method [Landi 2022]. Linearity for each Tauc plot had an R^2 of 0.99 or greater. The Kubelka-Munk function is defined as $F(R)=K/S$. The ratio can be calculated with equation 5:

$$\frac{K}{S} = \frac{(1-R)^2}{2R} \quad [5]$$

Where R is the reflectance, and K and S are the Kubelka-Munk absorption and scattering coefficients, respectively. However, to determine the band gap with a Tauc plot, the function is multiplied by energy and then set to the power of $1/p$ and graphed against energy. P equals 0.5 for dipole-allowed transitions at a direct band gap, equals 2 for dipole-allowed transitions near an indirect band gap, equals 1.5 for dipole-forbidden transitions at a direct band gap, or equals 3 for a dipole-forbidden transition near an indirect band gap [Landi 2022]. For the case of titanium dioxide anatase, p equals 2. Energy was calculated with equation 6.

$$E = \frac{hc}{\lambda} \quad [6]$$

where h is plank's constant, c is the speed of light, and λ is the wavelength. An example calculation can be seen in Appendix 4.

Chapter 3. RESULTS

3.1 TiO₂ co-doped with copper and iron

The co-doped nanoparticles were synthesized as described in chapter 2. The product formed from when the titanium was added before the metals is referred to as Ti + M and the product where the copper and iron was added first is referred to as M + Ti. Additionally, the characterization described in chapter 2 was completed on the co-doped products and the controls, synthesized TiO₂ and calcined reagents mixture. The characterization is summarized in this chapter in figures and tables that will be further analyzed in chapter 4. The spectra from XRD were analyzed, showing that the particles were co-doped and resulted in a mixture of anatase and rutile. It also showed that the formation of anatase was favored when titanium was reacted before the addition of metals. The spectra from XRF shows that the co-doped products have significantly more iron than copper. When the copper and iron were added in the synthesis affects concentration of copper, but not iron, in the co-doped product. The SEM images show the morphology of the particles and the porous surface change as a result of co-doping. The DRS spectra shows that the order of metal addition in the synthesis affected the band gap energy, and therefore wavelength of absorption, of the co-doped products.

3.1.1 X-ray diffraction of co-doped TiO₂.

XRD patterns were measured to determine the crystal structures of titanium dioxide. For comparison, a reagents mixture of commercial titanium dioxide, iron (II, III) oxide, and copper (II) oxide was calcined in similar conditions to the synthesized titanium oxide. The XRD patterns for synthesized titanium dioxide, calcined reagents mixture, and the co-doped products can be seen in Figure 3.1. There are three main observations to be taken from Figure 3.1.

First, the co-doped products (red and blue lines) show a different pattern than the TiO_2 (black line). The main signal for TiO_2 is at 25° and this peak is considerably more intense than the rest of the peaks in the spectrum. In contrast, the main signal in the co-doped products is around 55° and is more proportional to the rest of the peaks in the spectra compared to the control spectra. Overall, there are more diffraction peaks in the spectra of the co-doped products than in the spectrum of the titanium dioxide control. Second, Figure 3.1 shows that both co-doped products (red and blue lines) have a similar diffraction pattern but have slight differences

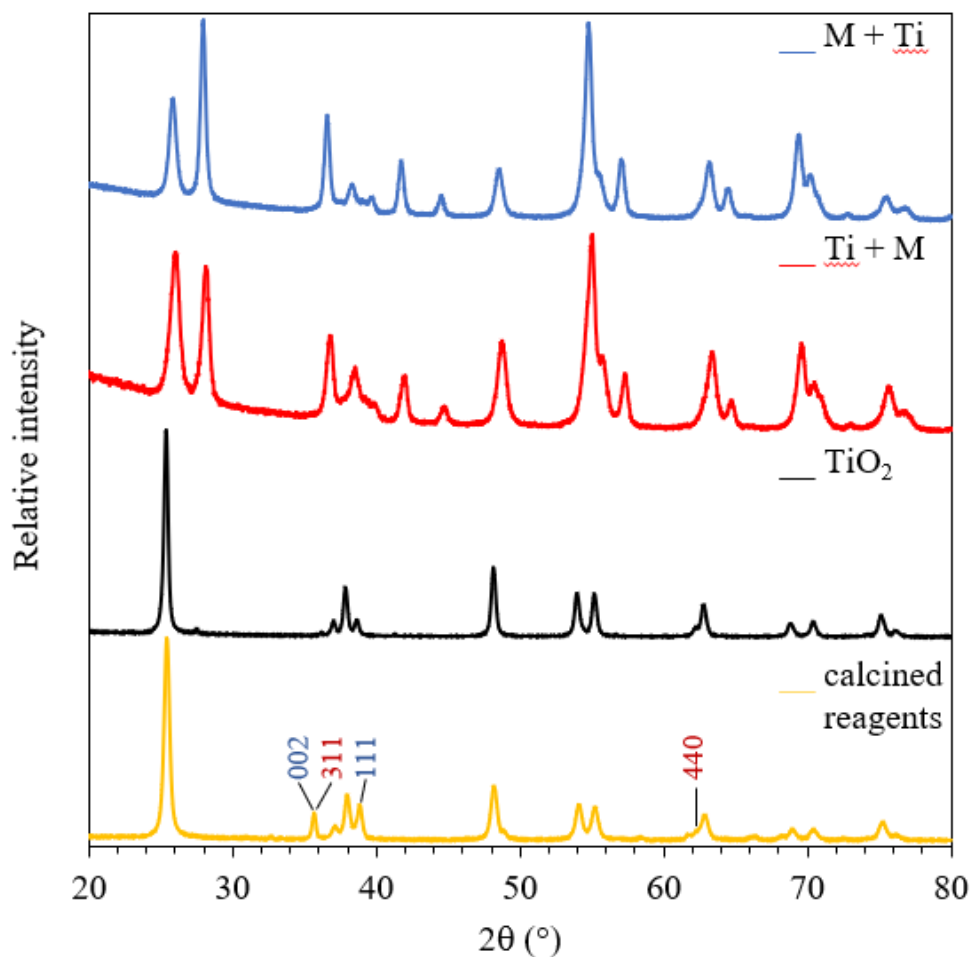


Figure 3.1. Offset XRD spectra of co-doped products, titanium dioxide control and calcined reagents. The main peak in each spectrum represents 100% intensity. Millar indices for CuO are in blue. Millar indices for Fe_3O_4 are in red.

in peak ratios depending on the step in which the copper and iron were introduced. For instance, the peaks around 26° and 28° are more equal in size when titanium is reacted before the introduction of copper and iron than when titanium is added after. Third, some diffraction peaks in the co-doped products (red and blue lines) match the diffraction pattern of TiO_2 (black line), and the unmatched peaks cannot be attributed to unreacted reagents (yellow line). For instance, the peak at 36° in the unreacted calcined reagents is not observed in the co-doped products. The lack of signal from iron oxide and copper oxide indicates that no crystal or agglomerate of these oxides is formed during the synthesis or calcination.

The peaks in Figure 3.1 that do not align with TiO_2 spectrum in the calcined reagents spectrum are a result of overlapping TiO_2 , CuO , and Fe_3O_4 peaks. The most intense peaks for CuO and Fe_3O_4 overlap at 36° , with Millar indices of 002 and 311 respectively [Etefagh 2013, Mishra 2015]. The second most intense peak for CuO is at 39° , Millar indices of 111, overlapping with a TiO_2 peak [Etefagh 2013]. The second most intense peak for Fe_3O_4 is at 63° , Millar indices of 440, overlapping with another TiO_2 peak, causing slight broadening [Mishra 2015]. The remaining lower intensity peaks for CuO and Fe_3O_4 are not observed [Etefagh 2013, Mishra 2015].

To identify the crystal structures of TiO_2 , the spectra were matched to the JCPDS reference spectra of anatase (JCPDS no. 84-1286) and rutile (JCPDS no. 88-1175), the main phases of TiO_2 . Figure 3.2 shows that the diffraction pattern of titanium dioxide control and calcined reagents correspond to the anatase crystal structure. The calcined reagents do not show rutile

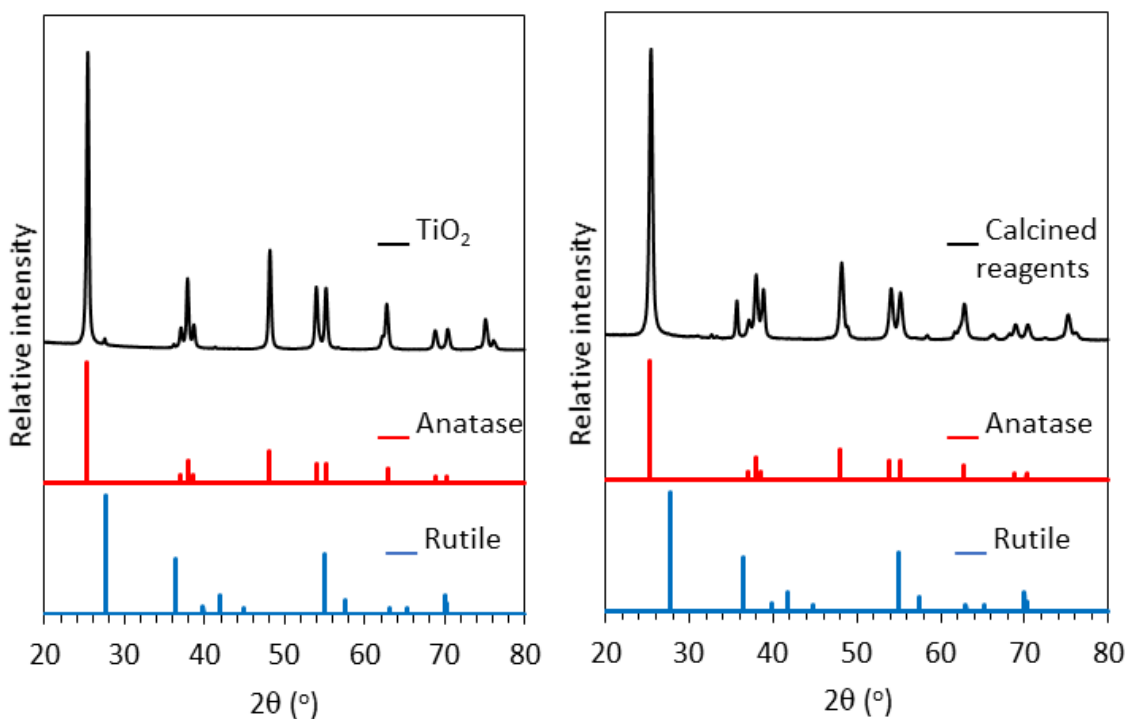


Figure 3.2. (left) Offset diffraction patterns of synthesized TiO₂ and reference anatase and rutile. (Right) Offset diffraction patterns of calcined reagents and reference anatase and rutile.

peaks, this titanium oxide was commercial anatase. For the calcined reagents, even though the peak at 36° coincides with one of the peaks from rutile (Figure 3.2, right), the lack of the rutile peak at 28° allows us to say that there is not rutile in the calcined reagents and is CuO and Fe₃O₄ overlap peak instead. The titanium dioxide control shows a tiny peak at 28° (Figure 3.2, left), indicating that small amount of rutile can be produced in the synthesis.

The JCPDS reference spectra were also compared to the co-doped products in Figure 3.3. The reference material shows that the peaks at 26° and 28° are the more intense for anatase and rutile, respectively, these peaks correspond to the 101 facet of anatase and 110 facet of rutile.

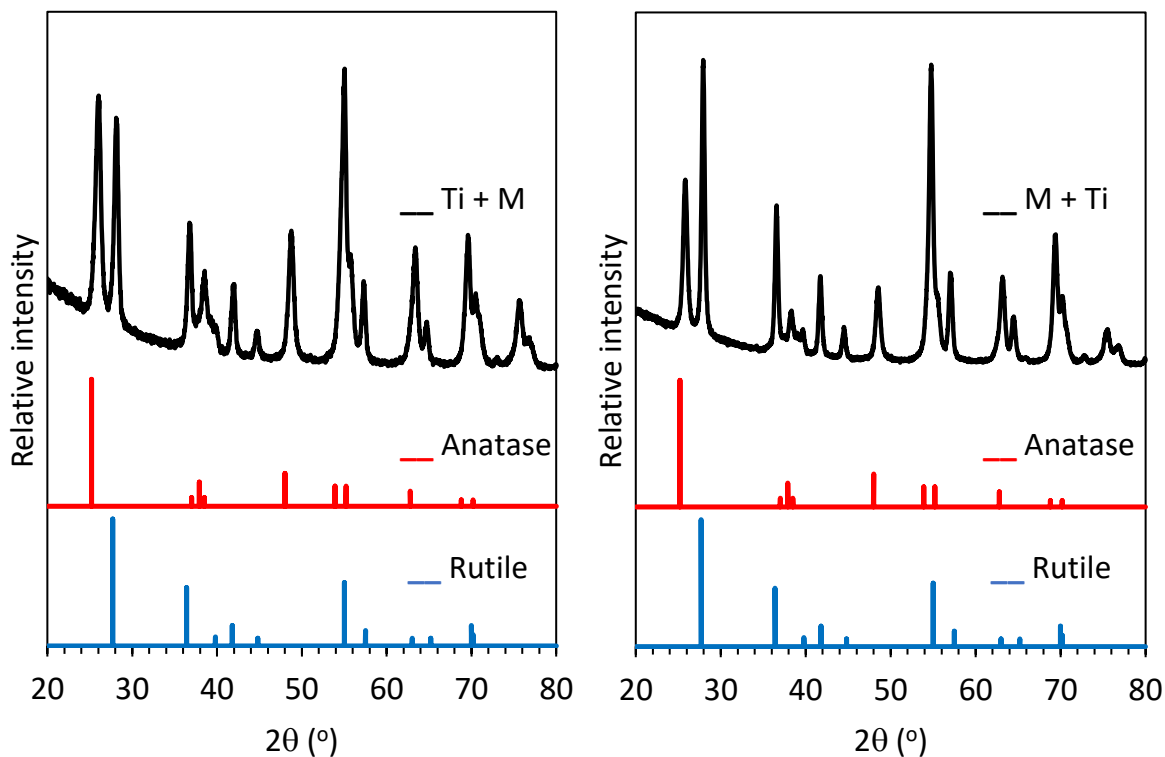


Figure 3.3. (left) Offset diffraction patterns of Ti + M co-doped product (added metals after the titanium) and reference anatase and rutile. (Right) Offset diffraction patterns of M + Ti co-doped product (added metals before the titanium) and reference anatase and rutile.

Table 3.1. Anatase's lattice parameters and grain size for titanium oxide control, calcined reagents, and co-doped products.

Sample	TiO ₂	Calcined reagents	Ti + M	M + Ti
d (101)	0.35092	0.35051	0.34217	0.34477
d (200)	0.18883	0.18879	0.18661	0.1874
a=b	0.37766	0.37758	0.37322	0.37480
c	0.94957	0.94372	0.85687	0.87905
Grain Size (nm)	21 ± 1	15 ± 6	9 ± 8	15 ± 5

These correspond to the most exposed facets of the crystal [Challagulla 2017]. However, the most intense peak in the co-doped product is at 55° . This is likely an overlap of anatase and rutile peaks with facets 105 and 211 for anatase and 220 for rutile [Thambiliyagodage 2021]. Additionally, the figure shows all the peaks have a slight shift towards larger angles compared to the reference anatase and rutile spectra.

The spectra were used to calculate the lattice parameters and average grain size summarized in Table 3.1. The lattice parameters were calculated using equations 2 and 3. The calculated distance between adjacent lattice planes (d) is the same for the controls, TiO_2 and calcined reagents. The shift in spectra for the co-doped products translated to a difference in the calculated distance between adjacent lattice planes (d) compared to the controls. The difference was greater for the Ti + M product than for the M + Ti product. The lattice parameters a/b and c were the same for the controls. The c values of the co-doped products were similar. The c values for the co-doped products were smaller than that of the controls, with the Ti + M product differing more than the M + Ti. The grain size, also summarized in Table 3.1, was calculated using equation 1. The Ti+M co-doped product appears to have a smaller average grain size than the controls and M + Ti co-doped product, however the error overlaps.

Using the spectra in Figure 3.3, the percent composition of anatase and rutile. The percentages were calculated using the peaks at 28° for rutile and 26° for anatase with the Spurr equation (Equation 4). As summarized in Table 3.2, the titanium dioxide control was found to contain 2% rutile. The resulting calculations for the doped products have a ratio of 1:1 ratio of anatase to rutile for the Ti+M co-doped product, while the M+Ti co-doped product has a 1:2 ratio of anatase to rutile crystal structures. The figure shows that an increase in rutile formation is a result of the doping metals being added and is not caused by experimental conditions.

Table 3.2. Percent of anatase and rutile in titanium dioxide control and co-doped products calculated from the main diffraction peak (facets shown in parenthesis).

Sample	% Anatase (101)	% Rutile (110)
TiO ₂	98	2
Ti + M	48	52
M + Ti	30	70

3.1.2 X-ray fluorescence of co-doped TiO₂

XRF was used for elemental analysis. Figure 3.4 shows the XRF spectra for calcined reagents (yellow), titanium dioxide (black) and co-doped products from Ti + M (red) and M + Ti (blue). The main signals observed come from titanium (Figure 3.4, left panel). The signals from iron (middle panel) and copper (right panel) are very small in comparison to the signals from the calcined reagents, but more similar in intensity to the iron and copper signals for titanium dioxide control. For intensity corrections and analysis, only the K_{α1} emissions were considered as these are more intense and do not overlap with other signals; these are the signals at 4.9 keV for titanium, 6.4 keV for iron, and 8.0 keV for copper, shown in Table 3.3. The noise of the spectra, 29 intensity units, was calculated as the standard deviation of the signal between 5.5 and 6.0 keV. The complete XRF data is summarized in Appendix 5.

Table 3.3 shows that both iron and copper were present in the co-doped products. The iron intensity increased by 269 in Ti + M, and 260 in M + Ti compared to titanium dioxide control. In comparison, the copper intensity increased more with a difference of 562 in Ti + M and 473 in M + Ti compared to titanium dioxide control. Both co-doped products show similar intensity for iron signal; considering that noise is 29 intensity units, these values show that similar amounts of

iron were incorporated in both co-doped products. In contrast, the intensity of the copper signal is approximately 5% larger in Ti + M than in M + Ti.

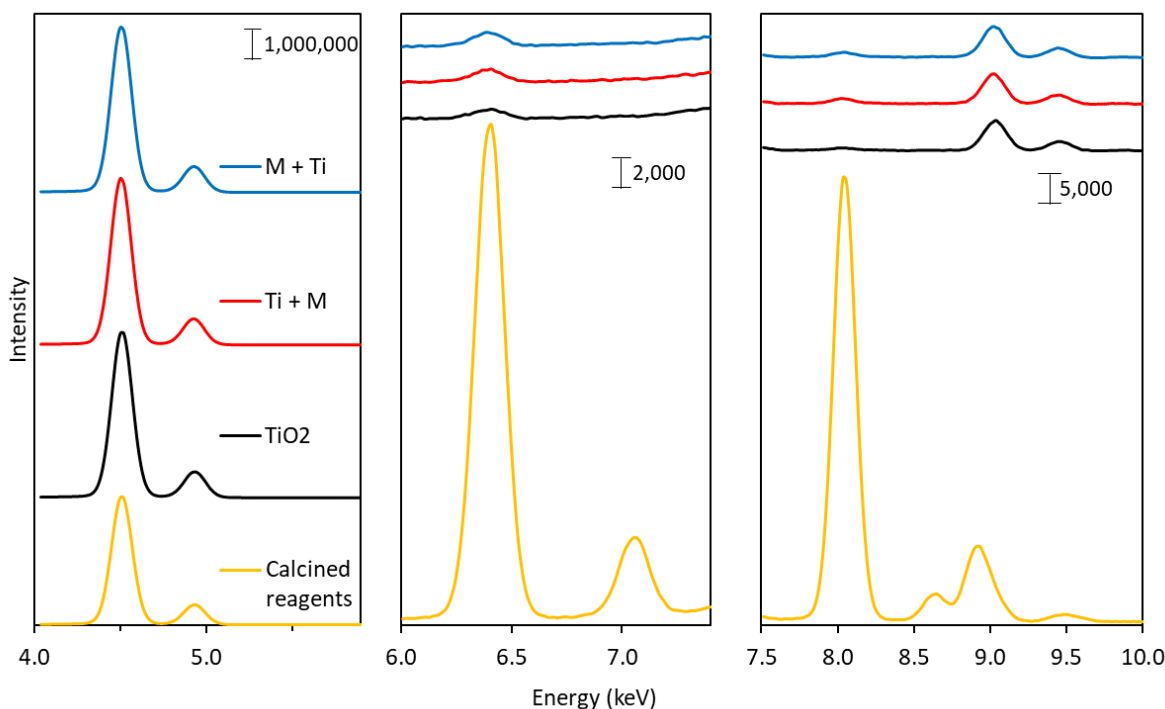


Figure 3.4. XRF spectra of calcined reagents (yellow), titanium dioxide control (black), and co-doped products from Ti + M (red) and M + Ti (blue). Peaks attributed to titanium are at 4.499 and 4.921 keV, iron are at 6.407 and 7.070 keV, and copper are at 8.034 and 8.918 keV.

Table 3.3. Intensity of titanium, iron, and copper at K energy levels for the titanium dioxide control, calcined reagents, and co-doped products. Noise = 29 intensity units. Full XRF data in Appendix 5.

Element energy level	Energy (keV)	Intensity calcined reagents	Intensity TiO ₂ control	Intensity Ti + M	Intensity M + Ti
Ti K _{α1}	4.499	502,690	646,704	653,016	649,314
Fe K _{α1}	6.407	35,291	1,382	1,651	1,642
Cu K _{α1}	8.034	95,191	1,432	1,994	1,905

A direct comparison between the signal of iron and copper is not possible as these elements have different sensitivity; however, relative comparison can be done since the iron and copper molar proportion is known for the calcined reagents. The intensities from the calcined reagents (Table 3.3) were used to obtain that the signal of copper is 2.7 time larger than the signal of iron (Appendix 6). Using this factor, the molar ratio Fe:Cu is 2.2 in the Ti + M co-doped product and 2.3 in the M + Ti co-doped product. This indicates that more iron is doped into the crystal than copper and that the amount of iron that is doped doesn't depend on the order of metal addition, but copper does.

3.1.3 Scanning electron microscopy of co-doped TiO₂

SEM was used to analyze the surface morphology of the nanoparticles. As seen in the SEM images in Figure 3.5A, titanium dioxide nanoparticles are spherical in nature. The calcined reagents resulted in particles that appear to have a fuzzy texture (Figure 3.5 B). The co-doped products also appeared heavily textured, appearing cracked and/or pitted (Figure 3.5 C and D).

3.1.4 Diffuse reflectance spectroscopy of co-doped TiO₂

DRS was used to measure the percent reflectance of each sample in order to calculate the estimated band gap wavelength and energy. Band gaps were obtained from the reflectance data using the Kubelka-Munk function and Tauc plot method. The DRS spectra with corresponding Tauc plots and images of the controls can be seen in Figure 3.6, and co-doped products in Figure 3.7. The band gap wavelength and energy are summarized in Table 3.4.

The commercial TiO₂ is the anatase used to prepare the calcined reagents, while the titanium dioxide control is obtained by our synthesis. Table 3.4 shows that all synthesized products have lower band gap energies than the commercial TiO₂. The calcined reagents, which also contain commercial TiO₂, show a band gap energy lower than the commercial TiO₂ sample. The co-

doped products have the lower band gap energy, with the lowest band gap energy obtained when titanium is reacted before the metals. The DRS data shows that the step in which the metals are added in the synthesis affects the band gap energy, and therefore absorption wavelength, of the co-doped products.

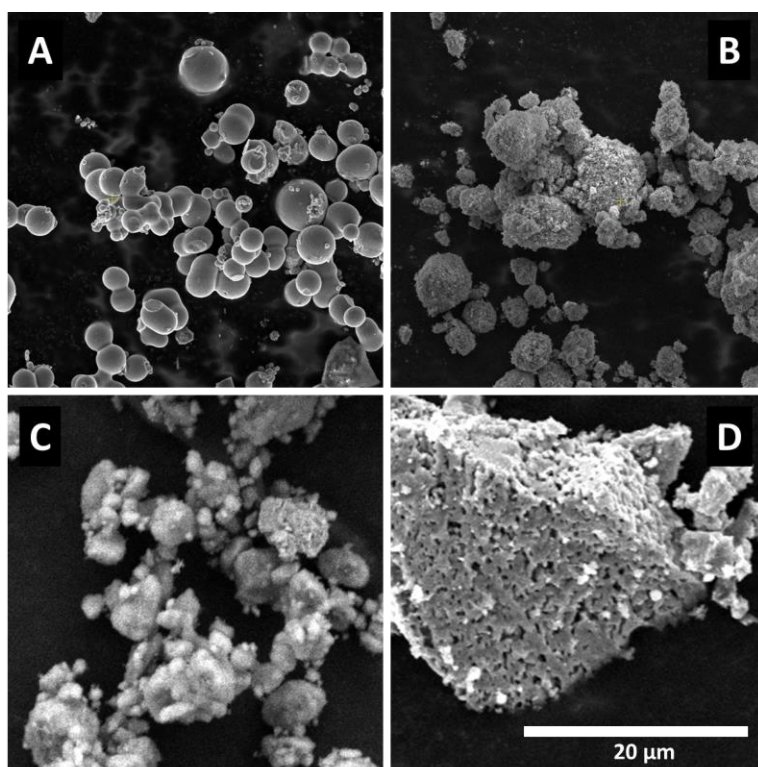


Figure 3.5. SEM images of (A) titanium dioxide control, (B) calcined reagents, (C) Ti+M co-doped product, and (D) M+Ti co-doped product. Scale bar apply to all micrographs.

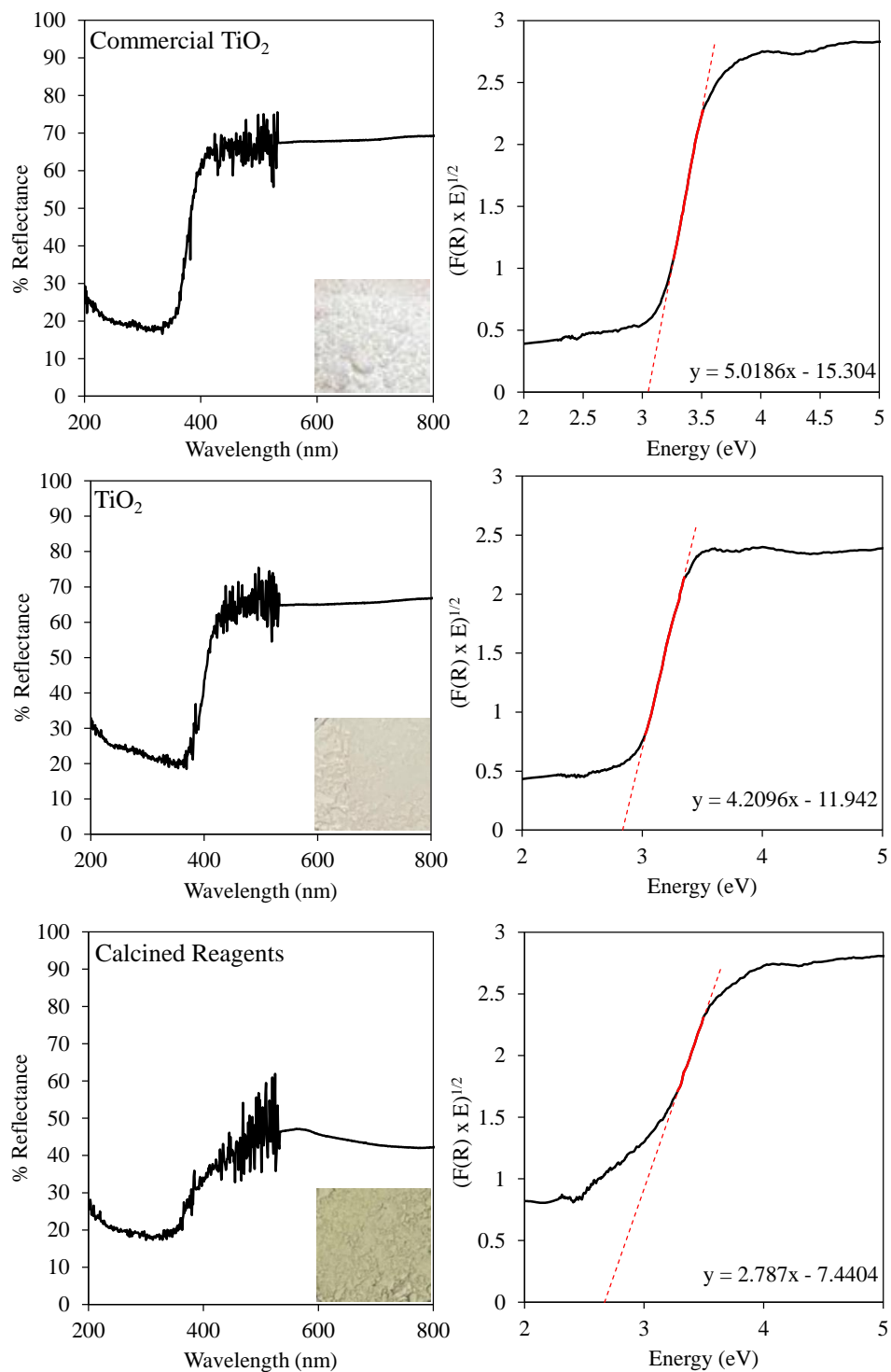


Figure 3.6. (Left) DRS spectra with photograph, and (right) corresponding Tauc plots showing extrapolation and linear regression equation for (top) commercial TiO_2 , (middle) titanium dioxide control, and (bottom) calcined reagents. All were measured with R^2 values greater the 0.99.

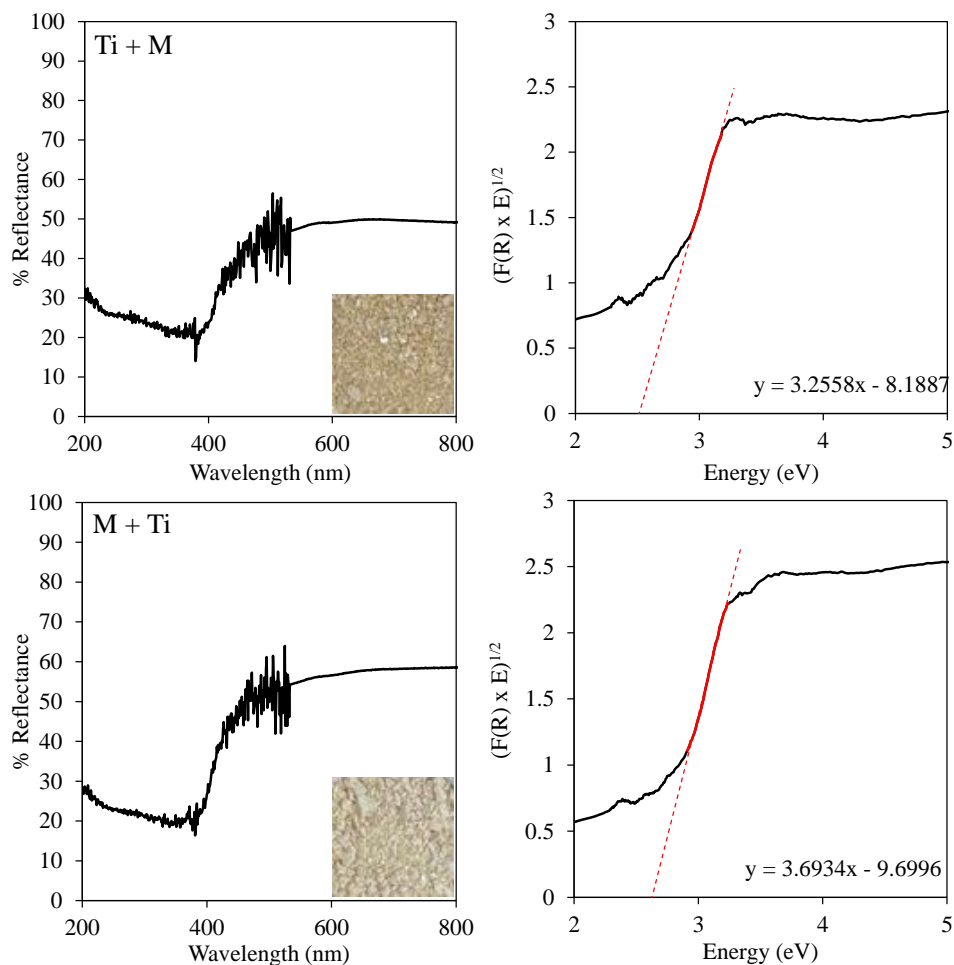


Figure 3.7. (Left) DRS spectra with photograph, and (right) corresponding Tauc plots showing extrapolation and linear regression for co-doped product (top) Ti + M and (bottom) M+ Ti. All were measured with R^2 values greater than 0.99.

Table 3.4. Summary of band gap wavelength and energy for reagents and co-doped products.

Sample	Band gap	
	λ (nm)	Energy (eV)
Commercial TiO_2	407 ± 7	3.050 ± 0.003
TiO_2 control	440 ± 10	2.837 ± 0.002
Calcined reagents	464 ± 3	2.671 ± 0.006
Ti + M	493 ± 4	2.517 ± 0.005
M + Ti	472 ± 4	2.628 ± 0.005

3.2 TiO₂ doped with copper

The copper doped nanoparticles were synthesized as described in chapter 2, without the addition of iron. The product formed from when the titanium was added before the copper is referred to as Ti + Cu and the product where the copper was added first is referred to as Cu + Ti. Again, the characterization described in chapter 2 was completed on the doped products and compared to the controls, titanium dioxide control and calcined reagents mixture. The spectra from XRD were analyzed, showing that the particles were doped and the formation of anatase, but not rutile. This, copper doping affected the size of the crystals, but not the crystallinity. The spectra from XRF shows that without the addition of iron, the concentration of copper does not change with the order of addition. The SEM images show that the surface of the copper doped nanoparticles is less porous than the co-doped. The DRS spectra shows that the order of metal addition in the synthesis affected the band gap energy and wavelength of the copper doped products.

3.2.1 X-ray diffraction of copper doped TiO₂

The XRD spectra of Ti + Cu and Cu +Ti can be seen in Figure 3.8. The peaks seen are indicative, in position and ratio, to anatase structure. Broad peaks are a result of small particle size, as supported with Table 3.5. The average particle was less than 4 nm. Table 3.5 also includes the lattice parameters for the doped products, which are similar in a/b, but different for c and d compared to the titanium dioxide control and calcined reagents. For the Ti + Cu product, c and d increased compared to the controls. In contrast, for the Cu + Ti product, c and d decreased compared to the controls.

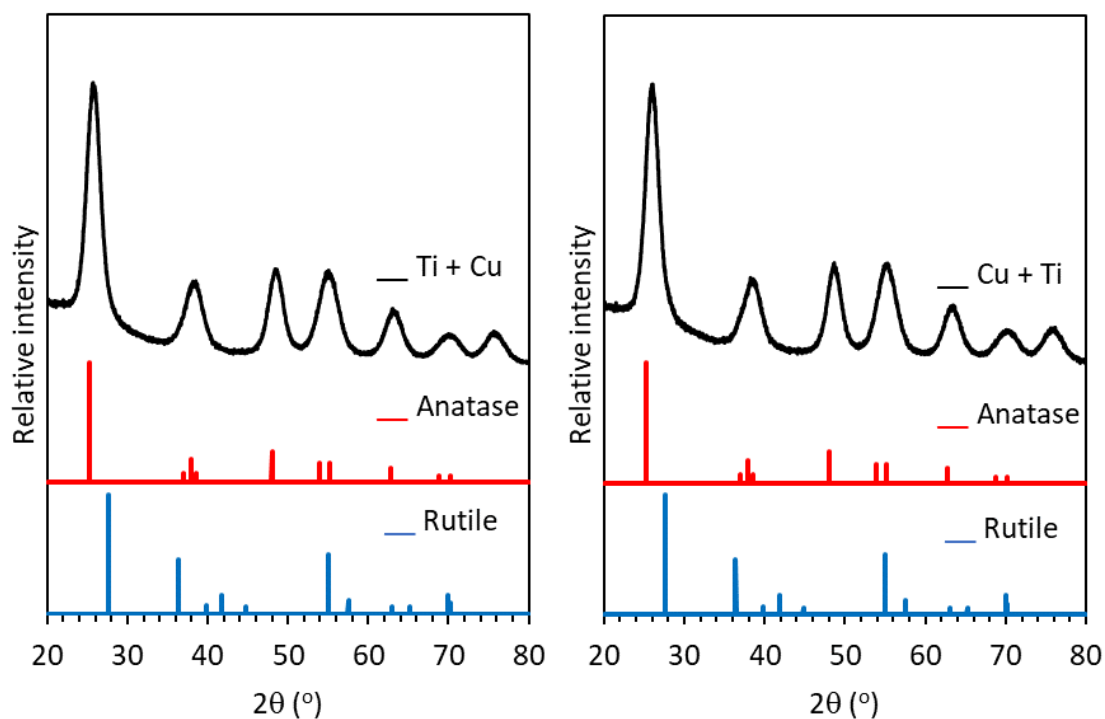


Figure 3.8. (left) Offset diffraction patterns of doped product from Ti + Cu synthesis (adding metals after titanium has been reacted) and reference anatase and rutile. (Right) Offset diffraction patterns of doped product from Cu + Ti synthesis (adding metals and titanium together) and reference anatase and rutile.

Table 3.5. Anatase's lattice parameters and grain size for TiO₂, calcined reagents, and copper doped TiO₂.

Sample	TiO ₂ control	Calcined reagents	Ti + Cu	Cu + Ti
Grain Size (nm)	21 ± 1	15 ± 6	2 ± 2	3.4 ± 0.5
a=b	0.37766	0.37758	0.37751	0.37721
c	0.94957	0.94372	0.97150	0.88298
d (101)	0.35092	0.35051	0.35188	0.34689
d (200)	0.18883	0.18879	0.18876	0.18861

3.2.2 X-ray fluorescence of copper doped TiO₂

The XRF data for copper doped products can be seen in Figure 3.9. The $K_{\alpha 1}$ peaks at 8.0 keV are small. However, Table 3.6 shows an increase in intensity of 517 for both Ti + Cu and Cu +Ti compared to titanium dioxide. Meaning that the amount of copper incorporated in the product was not affected by the order of the steps in the synthesis. This result is opposite to the previous observation that the amount of copper is incorporated in the co-doped product depends on the step in which the metal is introduced in the synthesis. The amount of copper in the doped product is less than in Ti + M co-doped product, but more than in M + Ti co-doped product. Since iron was not added, the signal of iron falls within the noise, and it is not different from the signal in titanium dioxide control.

3.2.3 Scanning electron microscopy of copper doped TiO₂

Copper doped particle SEM images, seen in Figure 3.10, show more pitted and cracked texture on the particle, and appear less porous than to the co-doped nanoparticles.

3.2.4 Diffuse reflectance spectroscopy of copper doped TiO₂

DRS spectra, Tauc plots, and images for copper doped products can be seen in Figure 3.11. The band gap wavelengths and energies were calculated for the samples in Figure 3.11 and summarized in Table 3.7. The band gap energies of products doped with copper are lower than the energy of the titanium dioxide control. The addition of copper before titanium produced the same band gap as the calcined reagents, while adding copper after titanium produced a larger band gap than the calcined reagent, a similar effect observed for the co-doped products.

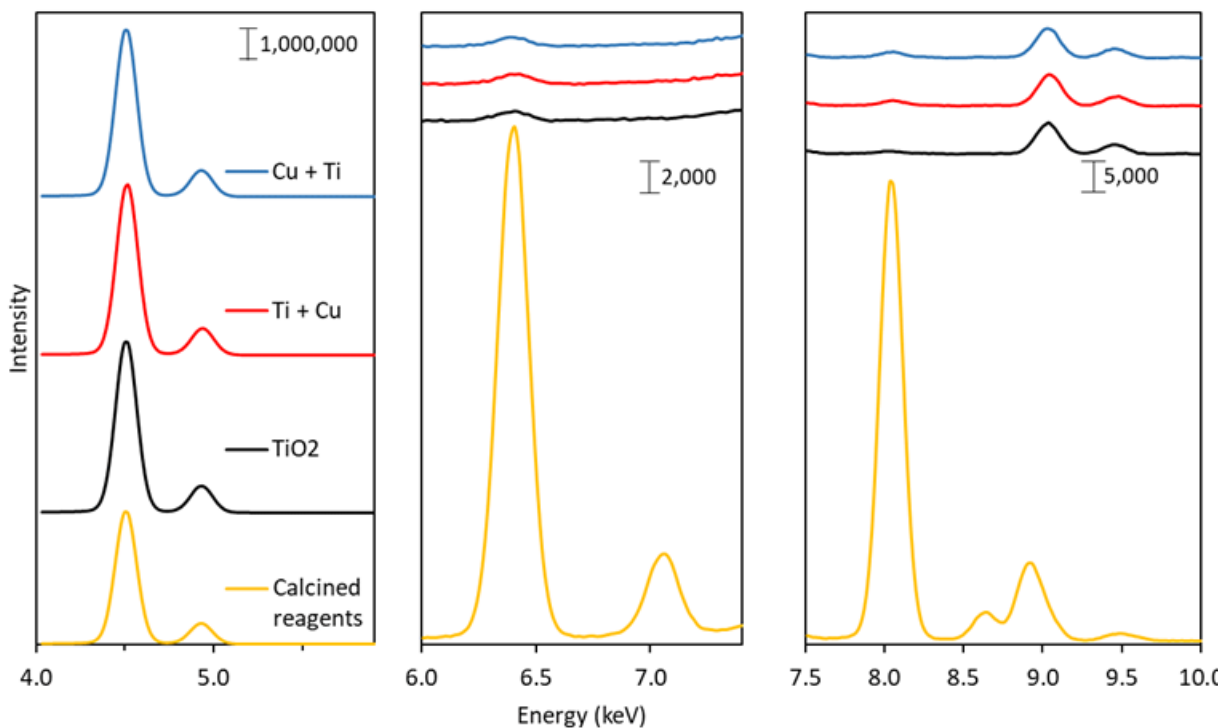


Figure 3.9. XRF spectra of calcined reagents (yellow), titanium dioxide control (black), and doped products from Ti + Cu (red) and Cu + Ti (blue). Peaks attributed to titanium are at 4.499 and 4.921 keV, iron are at 6.407 and 7.070 keV, and copper are at 8.034 and 8.918 keV.

Table 3.6. Intensity of titanium, iron, and copper at K energy levels for the titanium dioxide control, calcined reagents, and copper doped products. Noise = 29 intensity units. Full XRF data in Appendix 5.

Element energy level	Energy (keV)	Intensity Calcined Reagents	Intensity TiO ₂ control	Intensity Ti + Cu	Intensity Cu + Ti
Ti K _{α1}	4.499	502,690	646,704	628,877	629,433
Fe K _{α1}	6.407	35,291	1,382	1,360	1,360
Cu K _{α1}	8.034	95,191	1,432	1,949	1,949

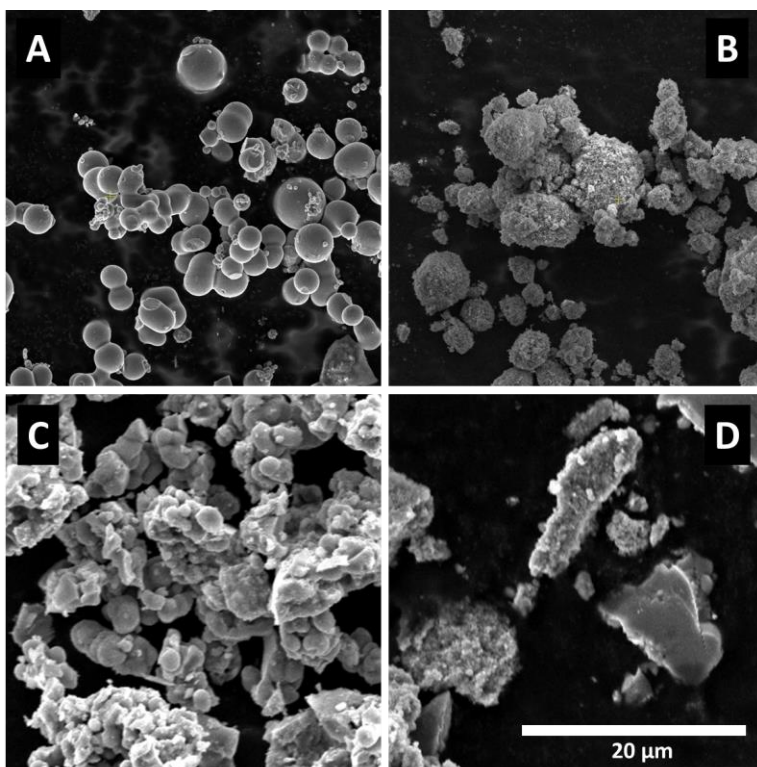


Figure 3.10. SEM images of (A) titanium dioxide control, (B) calcined reagents, (C) Ti + Cu, and (D) Cu + Ti doped product. Scale bar apply to all micrographs.

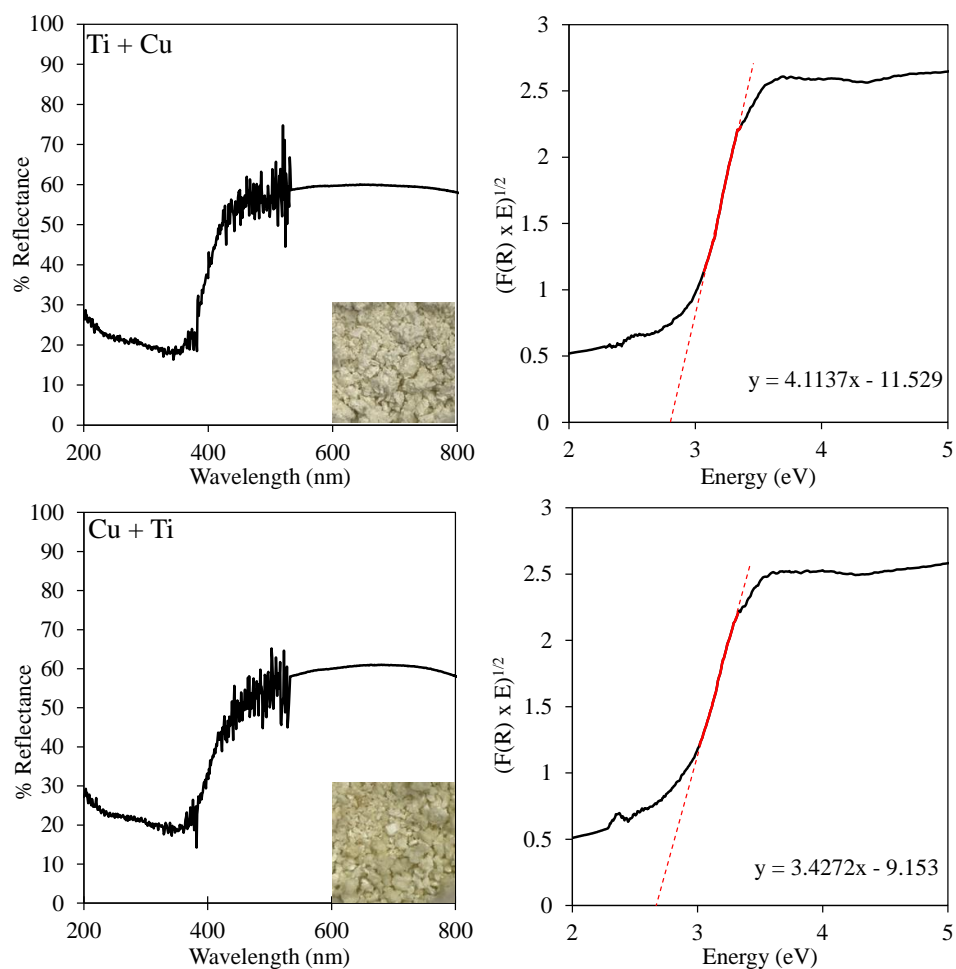


Figure 3.11. (Left) DRS spectra with photograph and (right) corresponding Tauc plots showing extrapolation and linear regression equation for doped product (top) Ti + Cu and (bottom) Cu + Ti. All were measured with R^2 values greater than 0.99.

Table 3.7. Summary of wavelength and band gap energy for reagents and copper doped products.

Sample	Band gap	
	$\lambda(\text{nm})$	Energy (eV)
Commercial TiO_2	407 ± 7	3.050 ± 0.003
TiO_2 control	440 ± 10	2.837 ± 0.002
Calcined reagents	464 ± 3	2.671 ± 0.006
Ti + Cu	450 ± 4	2.755 ± 0.005
Cu + Ti	464 ± 5	2.672 ± 0.004

3.3 TiO₂ doped with iron

The iron doped nanoparticles were synthesized as described in chapter 2, but without the addition of copper. The product formed from when the titanium was added before the iron is referred to as Ti + Fe and the product where the iron was added first is referred to as Fe + Ti. The same characterization was completed on the doped products and compared to the controls. The spectra from XRD were analyzed, showing the formation of small anatase particles. This also indicates that iron doping affects the grain size, but not the crystallinity. The spectra from XRF shows that doped products are dependent on the order of addition when copper is not present. The SEM images show that the surface of the particles is less porous than the co-doped products. The DRS spectra shows that the order of metal addition in the synthesis affected the band gap energy and wavelength.

3.3.1 X-ray diffraction of iron doped TiO₂

The XRD spectra for iron doped products (Figure 3.12) shows anatase structure, indicating that rutile formation was not dependent on the addition of iron. Broad peaks are due to small particle size, as summarized in Table 3.8, where the average particle is equal to or less than 5 nm. The lattice parameters are also summarized in Table 3.8, where the iron doped products have a slightly larger a/b and d values than the titanium dioxide control and calcined reagents. Additionally, when the titanium is reacted first, the c value increases, however, if the iron is added first, the c value decreases in comparison to the controls.

A small peak is observed around 31°; while detectable (more than 3 times the noise), this peak is below the limit of quantification (10 times the noise) of the spectra. The noise was calculated as the standard deviation of the intensity between 20° and 22°. Because this peak is too close to the noise, it was not analyzed.

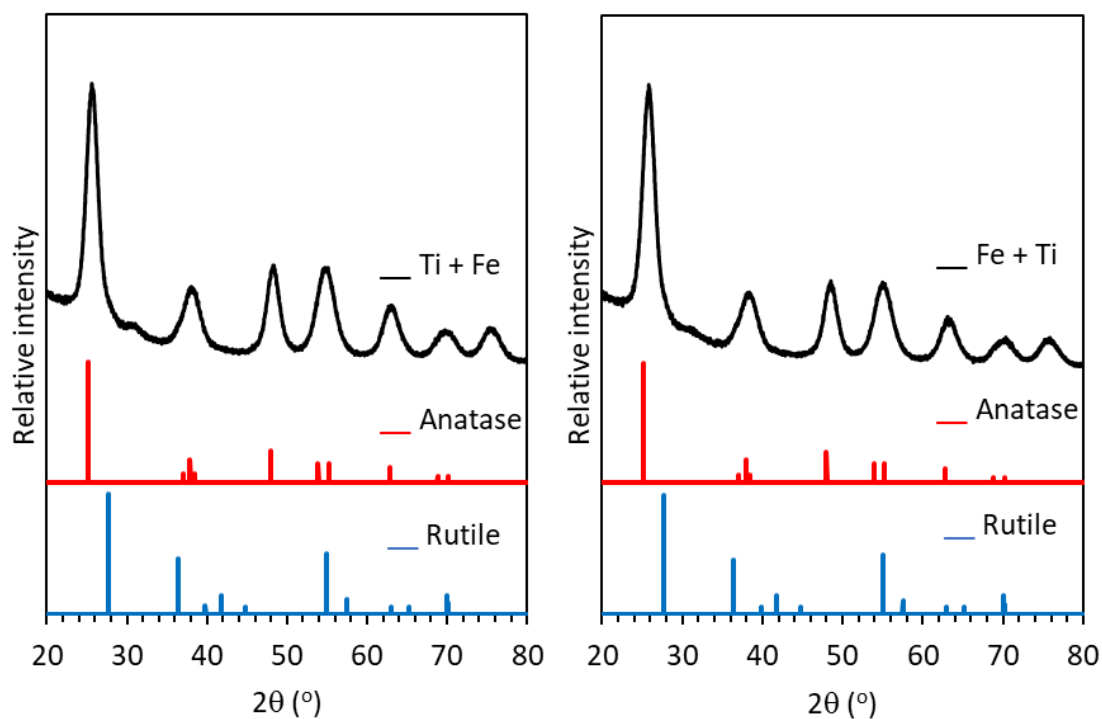


Figure 3.12. (left) Offset diffraction patterns of doped product from Ti + Fe synthesis (adding metals after titanium has been reacted) and reference anatase and rutile. (Right) Offset diffraction patterns of doped product from Fe + Ti synthesis (adding metals and titanium together) and reference anatase and rutile.

Table 3.8. Anatase's lattice parameters and grain size for TiO₂, calcined reagents, and iron doped TiO₂.

Sample	TiO ₂ control	Calcined reagents	Ti + Fe	Fe + Ti
Grain Size (nm)	21 ± 1	15 ± 6	5 ± 1	3 ± 3
a=b	0.37766	0.37758	0.37951	0.37817
c	0.94957	0.94372	0.95808	0.93625
d (101)	0.35092	0.35051	0.35284	0.35065
d (200)	0.18883	0.18879	0.18976	0.18909

3.3.2 X-ray fluorescence of iron doped TiO₂

The XRF spectra of iron doped products can be seen in Figure 3.13. The K_{α1} peaks at 6.4 keV are small. However, Table 3.9 shows an increase in intensity of 250 for Ti + Fe and 154 for Fe + Ti compared to titanium dioxide control. Meaning that the amount of iron incorporated in the product is affected by the order of the steps in the synthesis. This result is opposite to the previous observation that the amount of iron incorporated in the co-doped product was independent on the step in which the metal is introduced in the synthesis. Considering the noise of the spectra, the amount of iron in the co-doped products (Table 3.3) is the same than in the Ti + Fe doped product, but more than in the Fe + Ti doped product. Since copper was not added, the signal of copper is due to noise, and it is not different from the signal in titanium dioxide control.

3.3.3 Scanning electron microscopy of iron doped TiO₂

SEM images of iron doped products are seen in Figure 3.14. Some particles appear smooth, while others are bumpy or pitted

3.3.4 Diffuse reflectance spectroscopy of iron doped TiO₂

DRS spectra for iron doped products can be seen in Figure 3.15. Also shown in Figure 3.15 are images of the doped products. While there is a difference in coloration for both products, a larger difference is observed in the Fe + Ti product. The band gaps were calculated for those products and are summarized in Table 3.10. The band gap energies of products doped with iron are lower than the energy of the titanium dioxide control. The addition of iron before titanium produced a lower band gap than the calcined reagents, while adding iron after titanium, produced a larger band gap than the calcined reagents. DRS shows that, similarly to the co-doped products, the step in which the iron is added in the synthesis affects the band gap energy of the doped products.

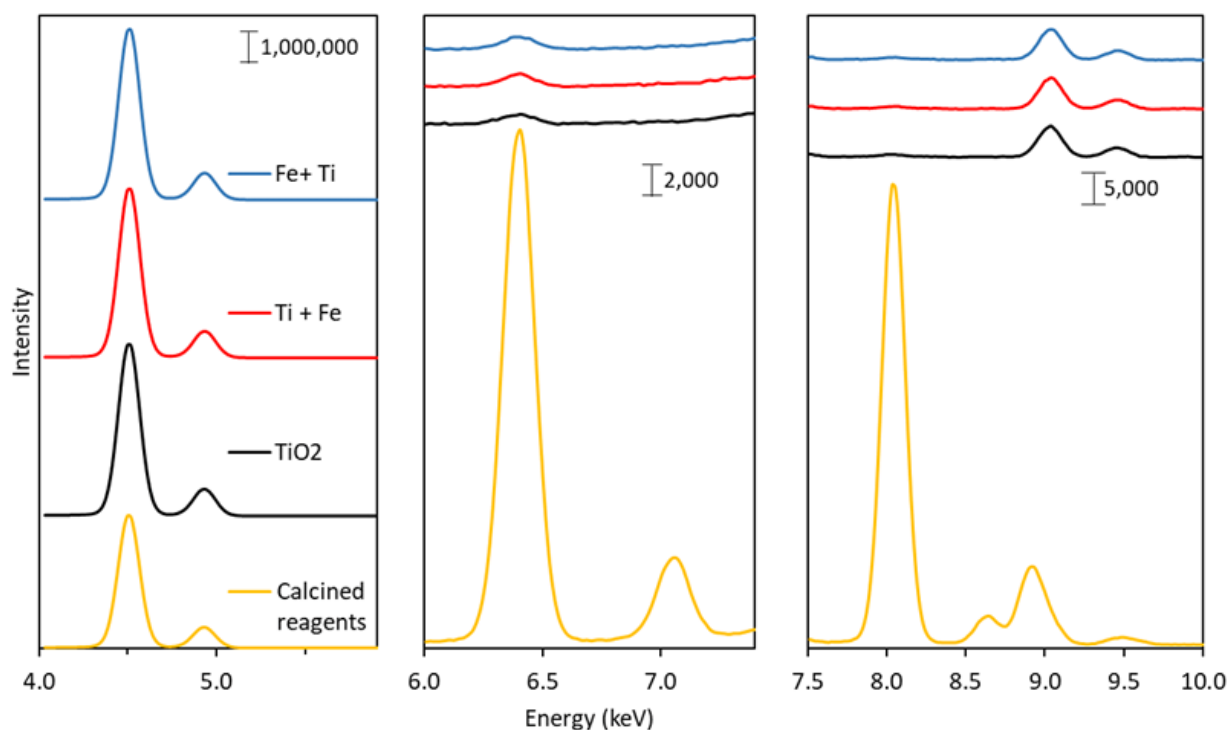


Figure 3.13. XRF spectra of calcined reagents (yellow), titanium dioxide control (black), and doped products from Ti + Fe (red) and Fe + Ti (blue). Peaks attributed to titanium are at 4.499 and 4.921 keV, iron are at 6.407 and 7.070 keV, and copper are at 8.034 and 8.918 keV.

Table 3.9. Intensity of titanium, iron, and copper at K energy levels for the titanium dioxide control, calcined reagents, and iron doped products. Noise = 29 intensity units. Full XRF data in Appendix 5.

Element energy level	Energy (keV)	Intensity Calcined Reagents	Intensity TiO ₂ control	Intensity Ti + Fe	Intensity Fe + Ti
Ti K_{α1}	4.499	502,690	646,704	635,142	639,393
Fe K_{α1}	6.407	35,291	1,382	1,632	1,536
Cu K_{α1}	8.034	95,191	1,432	1,371	1,362

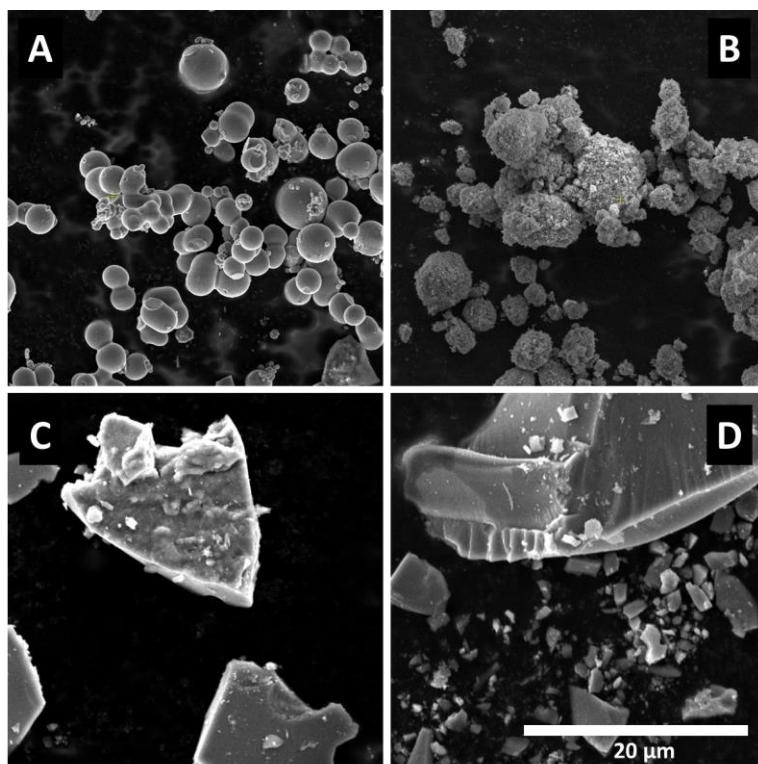


Figure 3.14. SEM images of (A) titanium dioxide control, (B) calcined reagents, (C) Ti + Fe, and (D) Fe + Ti doped products. Scale bar apply to all micrographs.

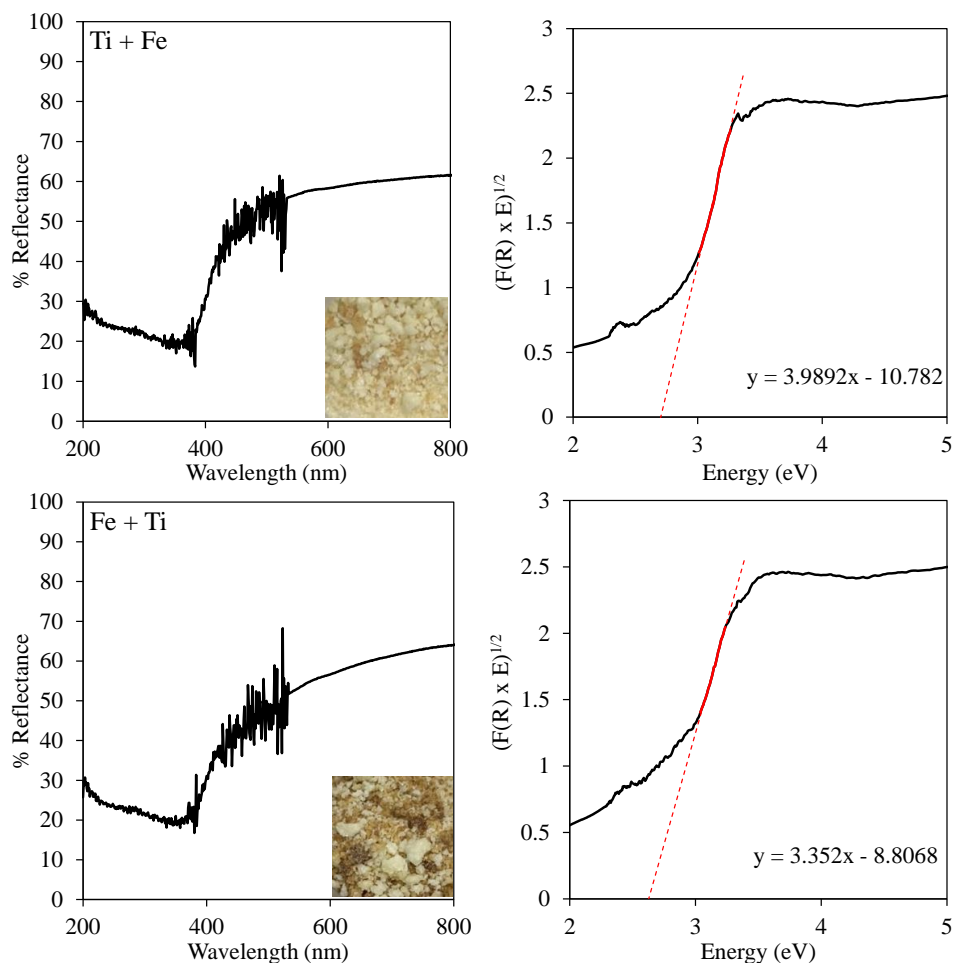


Figure 3.15. (Left) DRS spectra with photograph, and (right) corresponding Tauc plots showing extrapolation and linear regression for (top) Ti + Fe and (bottom) Fe + Ti doped products. All measured were with R^2 values greater than 0.99.

Table 3.10. Summary of wavelength and band gap energy for reagents and iron doped products.

Sample	Band gap	
	$\lambda(\text{nm})$	Energy (eV)
Commercial TiO_2	407 ± 7	3.050 ± 0.003
TiO_2 control	437 ± 10	2.837 ± 0.002
Calcined reagents	464 ± 3	2.671 ± 0.006
Ti + Fe	458 ± 3	2.705 ± 0.006
Fe + Ti	472 ± 3	2.629 ± 0.006

Table 3.11. Comparison of results by technique.

Synthesis	XRD	XRF	SEM	DRS
Ti + M	Anatase: Rutile 1:1 Smaller grain, smaller a, b, c, d than TiO ₂	Same amount of iron, but more copper than M + Ti	porous	Band gap is lower than M + Ti.
M + Ti	Anatase: Rutile 1:2	Same amount of iron, but less copper than Ti + M		Band gap is higher than Ti + M
Ti + Cu	Larger c than TiO ₂	Same amount of copper. Less amount of copper than Ti + M but more than M + Ti	Less porous than co-doped products	Band gap is higher than Cu + Ti, and higher than co-doped products
Cu + Ti	smaller c than TiO ₂			Band gap is lower than Ti + Cu, and higher than co-doped products
Ti + Fe	larger c and d than TiO ₂	More iron than Fe + Ti. Same than co-doped products	Less porous than co-doped products	Band gap is higher than Fe + Ti, and higher than co-doped products
Fe + Ti	smaller c and larger d than TiO ₂	Less iron than Ti + Fe. Less than co-doped products		Band gap is lower than Ti + Fe, and higher than co-doped products

Chapter 4. DISCUSSION

4.1 X-ray diffraction

Figure 3.2 was used to identify the crystal contents of the titanium dioxide control and co-doped products. The titanium dioxide control spectra compared to anatase and rutile spectra clearly shows anatase formation and some rutile formation. As mentioned, it was determined that the product was about 2% rutile. Rutile formation in the titanium dioxide control could be a result of increased temperature since anatase transforms into the thermodynamically metastable phase of rutile at temperatures of 600-700 °C [Hanaor 2011] as the pure TiO₂ product was calcined at 500 °C [Ismael 2020]. However, the lack of rutile peaks in the calcined reagents, which used a commercial TiO₂, indicates that calcination was not enough for the transformation, thus the traces of rutile observed in titanium dioxide control are not from the calcination and more likely come from the synthesis.

The calcined reagents show the anatase structure of TiO₂, copper (II) oxide peaks at 35° and 39°, and the main iron (II) oxide peak is at 48°, which is overlapped with an anatase peak. The main indication of CuO or Fe₃O₄ being present is a peak at 36°, but which oxide caused said peak is indistinguishable [Etefagh 2013, Mishra 2015]. When looking at Figure 3.1 for comparisons, peaks for copper (II) oxide are not observed in any other spectra.

Figure 3.3 shows the respective anatase and rutile peaks for the Ti + M and M + Ti co-doped products. Anatase and rutile were in a 1:1 ratio in the Ti+M co-doped product, but in a 1:2 ratio in the M+Ti co-doped product. The exact percentages of anatase and rutile in each product are shown in Table 3.2. The increased rutile formation agrees with the observation by Colón and coworkers that doping decreases the transition temperature from anatase to rutile [Colón 2006].

The shift of the diffraction peaks is a result of doping [Thambiliyagodage 2021]. To ensure that doping was successful, the lattice parameters, a , b , and c were calculated with Bragg's law with tetragonal configuration and the anatase peaks relating to 101 and 200 Miller indices at 25° and 45° . The results can be seen in Table 3.1. The calculations show a difference in lattice parameters when comparing the Ti + M or M + Ti parameters to the titanium dioxide control and calcined reagents. This is due to the distortion the copper and iron causes to the product, so a difference in lattice parameters indicates doping. Reacting titanium before adding the metals (Ti + M) resulted in smaller parameters, meaning more distortion of the anatase structure. The grain size was also calculated and summarized in Table 3.1. The co-doped products appear to be smaller than the controls; this observation agrees with previous report that increasing the amount of iron doping inhibits the growth of anatase [Hu 2020].

The XRD spectra of copper (Figure 3.8) and iron (Figure 3.12) doped TiO_2 shows that the products are only the anatase structure. Additionally, no copper or iron oxide peaks are observed. If doping with copper decreases the transition temperature between anatase and rutile, this effect was not enough to reach the experimental conditions (240°C). This means that the increased rutile formation observed in the co-doped products must be an effect of the addition of iron and copper doping together.

Doping was again confirmed by calculating the lattice parameters. All products showed a significant difference in parameters compared to the pure titanium dioxide and the calcined reagents, indicating the products were doped. A larger change is seen for copper doped products due to the size of the copper. However, since the iron dopes by replacing titanium in the crystal structure it distorts more of the parameters than copper, which does not replace titanium but rather fits in the interstitial spaces of the crystal [Byrne 2019]; these results agree with the

observation by Thambiliyagodage and Mirihana in which products doped with iron experienced more distortion than those doped with a similar concentration of copper [Thambiliyagodage 2021]. The broadening of the peaks is a result of the size that is shown in Table 3.5 and Table 3.8.

XRD analysis shows that doping with a single metal affects the lattice parameters of anatase. In contrast, co-doping results in a mixture of anatase and rutile and a change in parameters. Additionally, the formation of anatase is favored when titanium is added before copper and iron. It is suspected that the addition of titanium first allows for the formation of titanium dioxide nanoparticles in the anatase configuration before the metals are added. Then the addition of the metals encourages rutile formation, hence adding the metals first results in the percentage of rutile larger than the percentage of anatase, but there is still a portion of the Ti + M product that resulted in the rutile structure. The formation of iron or copper oxides was not observed.

4.2 X-ray fluorescence

Since copper and iron were added for doping in a low percentage of 0.05%, an increase in intensity for peaks attributed to copper and iron was small, as seen in Figure 3.4. Table 3.3 clearly shows an increase in intensity for copper and iron $K_{\alpha 1}$ energy levels, indicating the presence of copper and iron in the nanoparticles. The peak at 9.038 keV is a consequence of the detector where the signal for two Ti $K_{\alpha 1}$ levels from two different atoms is picked up by the detector as the sum of the two, equaling 9.038 keV. Peaks at 9.460 keV occur for a similar reason, as a sum of the Ti $K_{\alpha 1}$ level and the Ti $K_{\beta 1}$ level [Haschke 2014].

XRF shows that co-doped products have more iron than copper products. This difference may be consequence of the different ways in which the metals are incorporated in the crystal; as

mentioned, iron dopes by replacing titanium in the crystal structure, but copper fits in the interstitial spaces of the crystal [Byrne 2019]. Our observation is opposite to Thambiliyagodage and Mirihana, who found a 1:1 distribution of iron and copper, however, they do not correct for the difference in signal from each element [Thambiliyagodage 2021].

In the co-doped product, the steps of the synthesis affected the content of copper, but not of iron (Table 3.3). M + Ti contains both less anatase and less copper than Ti + M. This may be expected because rutile is a more compact crystal structure than anatase. Because of its larger size, copper doping is not replacement of Ti, but rather in the interstitial spaces of the crystal [Byrne 2019]. The anatase may accommodate a large ion and thus be more conducive to copper doping than rutile. [Hu 2020, Zang 2020]

Both syntheses with copper, Ti + Cu and Cu + Ti, showed the same increase of the copper signal (Table 3.6), suggesting that the amount of copper in the doped products is independent of the steps in which copper is introduced to the synthesis. In contrast, more iron was found in the doped product from Ti + Fe synthesis than in the Fe + Ti synthesis (Table 3.9), suggesting that the amount of iron in the doped products depends on the steps in which iron is introduced to the synthesis. These results are opposite to what was observed with the co-doped products, where the amount of copper, but not of iron, incorporated depended on the steps of the synthesis.

Given that anatase is the main crystalline structure obtained from the copper doping (Figure 3.8), the percent of copper incorporated in the crystal is only what can be incorporated in anatase crystals. The M + Ti co-doped product has a higher % of anatase and more copper than the Ti + M product. This suggests that different amounts of copper in the co-doped products is the result having a mixture of anatase and rutile (Table 3.1).

Given that anatase is the main crystalline structure obtained from the iron doping, we can say that these structures have different amounts of iron. Iron does induce the formation of rutile because of the similar size between iron and titanium ions [Hu 2020], consequently, we cannot make a correlation between the amount of iron and the percent of anatase or rutile in the product. The co-doped products are different mixtures of anatase and rutile and both show the same intensity of iron signal (Table 3.3). This intensity is similar to that from Ti + Fe, but larger than the signal from Fe + Ti (Table 3.9), even though both iron doped products are anatase. If this improvement of iron doping observed when titanium is reacted before adding the metal is also true for the co-doped reaction, the iron in the 48% anatase found in Ti + M product may be larger than the iron found in the 30% anatase found in M + Ti product, and in this way contribute to finding the same amount of iron in both co-doped products.

In summary, XRF shows that co-doping and single doping have opposite dependencies to the steps of the synthesis. The amount of copper in the product is dependent on the steps of the synthesis when iron is present, but independent when iron is absent. Opposite to copper's behavior, the amount of iron in the product is independent on the steps of the synthesis when copper is present, but dependent when copper is absent. These results support the idea that titanium dioxide particles in the anatase configuration form before the metals are added; however, doping depends on the cooperative effect of copper and iron together.

4.3 Scanning electron microscopy

As shown in Figure 3.5 the porosity is very different between the co-doped products. The morphologies being different than the calcined reagents and pure titanium dioxide is indicative of doping. The difference in porosity is likely due to the technique of synthesis since TiO_2

nanoparticles created with sol-gel technique is known to be porous, however the shape and dimension of the pores is very difficult to control [Babić 2016]. Babić et al. found that the porosity is strongly affected by the iron ions due to a number of unsaturated chemical bonds on the surface of the particle since Fe^{3+} is replacing some Ti^{4+} . The charge on the surface changes the packaging and agglomeration, which impacts the surface [Babić 2016]. Additionally, the incorporation of copper changes the morphology of the particle, as shown with lattice parameter calculations, leading to an irregular shape.

The images for the copper or iron doped products differ from the pure titanium dioxide and calcined reagents. Increased porosity has been observed for copper doped TiO_2 [Colón 2006]; however, single doped TiO_2 is less porous than co-doped products suggesting that the addition of the second ion increases the porosity of TiO_2 . As previously mentioned, this is due to a number of unsaturated chemical bonds on the surface of the particle, which changes the packaging and agglomeration, impacting the surface. Additionally, the nanoparticle shapes are inconsistent. Both factors indicate successful doping.

4.4. Diffusion reflectance spectroscopy

Commercially obtained anatase TiO_2 was used as a comparative sample for DRS. This was because the titanium dioxide control and the calcined reagents, which contains the commercially obtained anatase, would show a different band gap from rutile formation or the iron and copper oxides. The expected band gap for anatase is 3.2 eV, and the measured value was 3.050 ± 0.003 eV; this represents approximately 5% difference. Part of this difference in calculations can stem from band tails, where the density of energy levels between the valence and conduction band is not zero [Landi 2022]. Band tails states are electronic states just above the valence band or below

the conduction band arising from thermal, structural, impurity, and/or compositional disorder [Landi 2022]. This causes the band gap calculations to be smaller than expected since band tails cannot be estimated from DRS measurements [Landi 2022]. Additionally, Landi et al. found a decrease in band gap measurements if the thickness of the sample is too small. The Kubelka-Munk function assumes semi-infinite thickness. Since samples were measured with the goal of covering the quartz window in entirety, the thickness was likely near 0.5 mm. Landi et al. linked a decrease in band gap calculations for samples less than 1 mm thick compared to samples equal to or greater than 1 mm thick. Additionally, Thambiliyagodage and Mirihana identified both Ti^{4+} and Ti^{3+} in high resolution with the XPS spectra. They believe that a decrease in band gap can be due to the oxygen vacancies and localized gap states induced by Ti^{3+} . The missing oxygen could allow one or two electrons to be localized in an oxygen vacancy state that would then form a donor level below the conduction band, reducing the band gap [Thambiliyagodage 2021]. Finally, measurement bias is present when using the Tauc plot method. Measurements were taken by more than one individual and with R^2 greater than or equal to 0.99 in attempt to decrease that bias. However, even with a decrease in the calculated band gap compared to what was expected, the band gap relationship and trend remain the same.

The calcined reagents sample has a smaller estimated band gap of 2.671 ± 0.006 eV because the sample is a mixture, and the calculation is an average of all present band gaps. The expected band gaps of the reagents are about 3.2 eV for anatase, 2.4 eV for iron (II, III) oxide, and 2.4 eV for copper (I) oxide [Rahimi 2016, Serin 2005, Gillen 2013]. The anatase in the mixture had a calculated band gap of 3.050 ± 0.003 eV, so the difference to 2.671 ± 0.006 eV is a result of the averaged band gaps with iron (II, III) oxide and copper (I) oxide.

The titanium dioxide control had a slightly smaller band gap due to the introduction of rutile formation, as was shown with the XRD spectra. As mentioned, rutile has a band gap of about 3.0 eV. The introduction of rutile decreases the average calculated band gap to 2.837 ± 0.002 eV. The band gap is not between 3.2 eV and 3.0 eV for the same reasons the anatase calculated band gap differed from what was expected. However, the estimated band gap for the titanium dioxide control is within 0.2 eV of calculated anatase band gap as expected.

The single doped and co-doped products show a significant decrease in measured band gap compared to titanium dioxide control. The band gaps of Ti + M and M + Ti products are 0.533 eV and 0.422 eV, respectively, lower than that of commercial anatase. The band gaps of Ti + Cu and Cu + Ti products are 0.276 eV and 0.378 eV, respectively, lower than that of commercial anatase. The band gaps of Ti + Fe and Fe + Ti products are 0.345 eV and 0.421 eV, respectively, lower than that of commercial anatase. All these differences are outside the range of what rutile formation would be able to effect, therefore the decrease in band gap can be linked to the doping and co-doping of copper and iron.

For the single doping, copper or iron being added before the titanium allows for the doping metal to have more of an effect on narrowing the band gap than when added after the titanium. As previously mentioned, the copper dopes in the interstitial position which leads to oxygen vacancies, forming impurity states in the band gap, narrowing the gap. Since iron dopes by substituting the titanium, it is believed that a new energy level is formed below the conduction band due to the doping of iron and the formation of Ti^{3+} [Thambiliyagodage 2021, Byrne 2019]. For the co-doped product, the combined effects of the two metals allow that band gap to be decreased more than what can be attributed to rutile formation or to a single doping metal.

The largest wavelength of absorption was obtained for the co-doped products. This indicates that doped titanium dioxide in particulate matter would be able to absorb more solar radiation. This would increase the photocatalytic activity by increasing the number of excited electrons in the conduction band, and in turn increasing the reduction of iron in the matter.

The band gap responded differently to the steps of the synthesis depending on the number of metals used for doping. For single doping, the band gap was larger when the titanium was reacted before copper or iron. For co-doping, the band gap was smaller when the titanium was reacted before copper and iron. XRF showed that the amount of metal incorporated in the semiconductor also responded differently to the steps of the synthesis depending on the number of metals used for doping. This supports the idea that the behavior of doping metal is affected by the presence of another doping metal.

Ideally, more metal doping would result in a large shift of the band gap, this lower band gap values. This is true for the co-doped product, where $Ti + M$ has more metal content (Table 3.3) and the smallest band gap (Table 3.4). On the contrary, no correlation between the amount of metal and band gap shift was found in the single doped products. Even though both copper doped products have the same amount of copper (Table 3.6), adding the copper after titanium resulted in a larger band gap (Table 3.7) than adding the titanium after copper. For iron, $Fe + Ti$ had a smaller band gap (Table 3.10) and less amount of iron than $Ti + Fe$ (Table 3.9).

In summary, DRS shows that doping TiO_2 with iron and copper decreases its band gap, and co-coping further decreases the band gap. Similar to the content of doping metal, the band gap responded differently to the steps of the synthesis depending on the number of metals used for doping.

Chapter 5. CONCLUSIONS

Titanium dioxide is a promising photocatalyst that is already playing a role in the atmosphere. Its ability to act as a photocatalyst can trigger other reduction reactions of Fe^{3+} to Fe^{2+} in aerosols. The bioavailability of Fe^{2+} is important for ocean species, such as phytoplankton, and can be partially sourced from said aerosols. The photocatalytic property of titanium dioxide is increased in particles that contain copper, making it important to investigate. Other parameters, such as when the doping metals and the individual effects of the metals added play a role in the photocatalytic potential and were also investigated.

XRD analysis showed that doping with a single metal affected the parameters of anatase. In contrast, co-doping resulted in a mixture of anatase and rutile. Additionally, the formation of anatase was favored when titanium is added before copper and iron. It is suspected that the addition of titanium first allowed for the formation of titanium dioxide particles in the anatase configuration before the doping metals were added. Then the addition of the metals encouraged rutile formation, hence adding the metals first resulted in a percentage of rutile larger than the percentage of anatase, but there was still a portion of the $\text{Ti} + \text{M}$ product that resulted in the rutile structure. The formation of iron or copper oxides was not observed, indicating doping was successful.

XRF showed that co-doping and single doping have opposite dependences to the steps of the synthesis. The amount of copper in the product was dependent on the steps of the synthesis when iron was present, but independent when iron was absent. Opposite to copper's behavior, the amount of iron in the product was independent of the steps of the synthesis when copper was present, but dependent when copper was absent. These results support the idea that titanium

dioxide particles in the anatase configuration form before the metals are added; however, doping depended on the cooperative effect of copper and iron together.

The SEM images show the morphology of the particles and the porous surface changed as a result of doping, with more porous material obtained from co-coping than single doping.

In summary, DRS data showed that doping TiO_2 with iron and copper decreased its band gap, and co-coping further decreased the band gap. Similar to the content of doping metal, the band gap responded differently to the steps of the synthesis depending on the number of metals used for doping.

Some future studies could be done looking at the particles in tropospheric conditions, as well as particles made with different concentrations of doping metals and different calcining temperatures, and analyzing the ratio of iron II to iron III, photocatalytic capacity, and the surface area using BET. From this study overall, the co-doped product $\text{Ti} + \text{M}$ had the largest content of copper and iron, less percent rutile formation than $\text{M} + \text{Ti}$, the smallest band gap, and the largest wavelength. This indicates that doped titanium dioxide in particulate matter would be able to absorb more solar radiation. It is expected that the photocatalytic potential of titanium dioxide is increased as well. This supports the idea that atmospheric particles that contain iron and copper doped titanium dioxide could trigger redox reactions to reduce Fe^{3+} and form more bioavailable Fe^{2+} .

ACKNOWLEDGEMENTS

I want to give a huge thank you to Dr. Maryuri Roca for all of her assistance and advice while working through this project and throughout my time conducting research with her. I would also like to thank Dr. Juan Navea for his guidance and help reviewing this paper. I want to acknowledge Dr. Steven Frey, Lisa Quimby and Lily Kozel for their aid with instrumentation. Lastly, I want to thank the Skidmore Chemistry staff and peers that have helped and encouraged me throughout my time at Skidmore.

REFERENCES

- Babić B., Zarubica A., Arsića T.M., Pantića J., Jokić B., Abazović N., Matovića B. Iron doped anatase for application in photocatalysis. *Journal of the European Ceramic Society*. **2016**, 36, 2991-2996. <https://doi.org/10.1016/j.jeurceramsoc.2015.11.031>
- Bokov D., Jalil A.T., Chupradit S., Suksatan W., Ansari M.J., Shewael I.H., Valiev G.H., Kianfar E. Nanomaterial by Sol-Gel Method: Synthesis and Application. *Advances in Materials Science and Engineering* **2021**, 5102014. <https://doi.org/10.1155/2021/5102014>
- Borgatta J., Paskavitz A., Kim, D., Navea J.G. Comparative evaluation of iron leach from different sources of fly ash under atmospherically relevant conditions. *Environmental Chemistry* **2016**, 13, 902-912. <https://doi.org/10.1071/EN16046>
- Byrne C. Moran L., Hermosilla D., Merayo N., Blanco A., Rhatigan S., Hinder S., Ganguly P., Nolan M., Pillai S.C. Effect of Cu doping on the anatase-to-rutile phase transition in TiO₂ photocatalysts: Theory and experiments. *Applied Catalysis B: Environmental* **2019**, 246, 266-276. <https://doi.org/10.1016/j.apcatb.2019.01.058>
- Challagulla S., Tarafder K., Ganesa R., Roy S. Structure sensitive photocatalytic reduction of nitroarenes over TiO₂. *Scientific Reports* **2017**, 7, 1-11. <https://doi.org/10.1038/s41598-017-08599-2>
- Colón G., Maicu M., Hidalgo M.C., Navío J.A. Cu-doped TiO₂ systems with improved photocatalytic activity. *Applied Catalysis B: Environmental* 2006, 67, 41-51. <https://doi.org/10.1016/j.apcatb.2006.03.019>
- Drees L.R., Ulery A.L. (2008) Methods of Soil Analysis Part 5. Mineralogical methods. American Society of Agronomy. ISBN-13: 978-0891188469
- Etefagh R., Azhir E., Shahtahmasebi N. Synthesis of CuO nanoparticles and fabrication of nanostructural layer biosensors for detecting *Aspergillus niger* fungi. *Scientia Iranica* **2016**, 20, 1055-1058. <https://doi.org/10.1016/j.scient.2013.05.015>
- Gillen R., Robertson J. Accurate screened exchange band structures for the transition metal monoxides MnO, FeO, CoO and NiO. *Journal of Physics: Condensed Matter* **2013**, 25, 165502. doi:10.1088/0953-8984/25/16/165502
- Guzmán-Velderrain V., Ortega López Y., Salinas Gutiérrez J., López Ortiz A., Collins-Martínez V.H. TiO₂ Films Synthesis over Polypropylene by Sol-Gel Assisted with Hydrothermal Treatment for the Photocatalytic Propane Degradation. *Green and Sustainable Chemistry* **2014**, 120-132. DOI: 10.4236/gsc.2014.43017
- Hanaor D.A.H., Sorrell C.C. Review of the anatase to rutile phase transformation. *Journal of Material Science* **2011**, 46, 855–874. <https://doi.org/10.1007/s10853-010-5113-0>

Haschke M. (2014) Laboratory Micro-X-Ray Fluorescence Spectroscopy. Instrumentation and Applications. In Springer Series in Surface Sciences volume 55. SpringerLink. <https://doi.org/10.1007/978-3-319-04864-2>

Holder C.F., Schaak R.E. Tutorial on Powder X-ray Diffraction for Characterizing Nanoscale Materials. *ACS Nano* **2019**, 13, 7359-7365. <https://doi.org/10.1021/acsnano.9b05157>

Hu Z, Xu T., Liu P., Jin G. Developed photocatalytic semi-flexible pavement for automobile exhaust purification using iron-doped titanium dioxide. *Construction and Building Materials* **2020**, 262, 119924. <https://doi.org/10.1016/j.conbuildmat.2020.119924>

Ismael M. Enhanced photocatalytic hydrogen production and degradation of organic pollutants from Fe (III) doped TiO₂ nanoparticles. *Journal of Environmental Chemical Engineering* **2020**, 8, 103676. <https://doi.org/10.1016/j.jece.2020.103676>

Katal R., Masudy-Panah S., Tanhaei M., Davood M.H., Farahani A., Jiangyong H. A review on the synthesis of the various types of anatase TiO₂ facets and their applications for photocatalysis. *Chemical Engineering Journal* **2020**, 384, 123384. <https://doi.org/10.1016/j.cej.2019.123384>

Kim D., Xiao Y., Karchere-Sun R., Richmond E., Ricker H.M., Leonardi A., Navea J.G. Atmospheric processing of anthropogenic combustion particles: Effects of acid media and solar flux on the iron mobility from fly ash. *ACS Earth and Space Chemistry* **2020**, 4, 750-761. <https://doi.org/10.1021/acsearthspacechem.0c00057>

Lance R. Optical Analysis of Titania: Band Gaps of Brookite, Rutile and Anatase. Dissertation. Department of Physics, Oregon State University 2018. https://ir.library.oregonstate.edu/concern/undergraduate_thesis_or_projects/5t34sq67c

Landi S. Segundo, I. R.; Freitas, E.; Vasilevskiy, M.; Carneiro, J.; Tavares, C. J. Use and misuse of the Kubelka-Munk function to obtain the band gap energy from diffuse reflectance measurements. *Solid State Communications* **2022**, 341, 114573. <https://doi.org/10.1016/j.ssc.2021.114573>

Li H., Duan X., Liu G., Li L. Synthesis and characterization of copper ions surface-doped titanium dioxide nanotubes. *Materials Research Bulletin* **2008**, 43, 1971-1981. <https://doi.org/10.1016/j.materresbull.2007.10.005>

Lin J.C.T, Sopajaree K., Jitjanesuwan T., Lu M.C. Application of visible light on copper-doped titanium dioxide catalyzing degradation of chlorophenols. *Separation and Purification Technology* **2018**, 191, 233-243. <https://doi.org/10.1016/j.seppur.2017.09.027>

Mishra A., Sardar M. (2015) Isolation of genomic DNA by silane-modified iron oxide nanoparticles. In nanotechnology: novel perspectives and prospects. McGraw Hill Education, New York, pp.309-315. pdf

Nabi D., Aslam I., Qazi I. Evaluation of the adsorption potential of titanium dioxide nanoparticles for arsenic removal. *Journal of Environmental Sciences* **2009**, 21, 402-408. [https://doi.org/10.1016/S1001-0742\(08\)62283-4](https://doi.org/10.1016/S1001-0742(08)62283-4)

Oganisian K., Hreniak A., Sikora A., Gaworska-Koniarek W., Iwan A. Synthesis of iron doped titanium dioxide by sol-gel method for magnetic applications. *Processing and Application of Ceramics* **2015**, 9, 43-51. <https://doi.org/10.2298/PAC1501043O>

Ostaszewski C.J., Stuart N.M., Lesko D.M., Kim D., Lueckheide M.J., Navea J.G. Effects of coadsorbed water on the heterogeneous photochemistry of nitrates adsorbed on TiO₂. *The Journal of Physical Chemistry A* **2018**, 122, 6360-6371. <https://doi.org/10.1016/j.jphotochemrev.2012.10.001>

Park H., Park Y., Kim W., Choi W. Surface modification of TiO₂ photocatalyst for environmental applications. *Journal of Photochemistry and Photobiology C: Photochemistry Reviews* **2013**, 15, 1-20. <https://doi.org/10.1016/j.jphotochemrev.2012.10.001>

Pecharsky V.K., Zavalij P.Y. (2009) Fundamentals of Powder Diffraction and Structural Characterization of Materials, Second Edition. SpringerLink. <https://doi.org/10.1007/978-0-387-09579-0>

Pelaez M., Nolan N.T., Pillai S.C., Seery M.K., Falaras P., Kontos A.G., Dunlop P.S.M., Hamilton J.W.J., Byrne J.A., O'Shea K., Entezari M.H., Dionysiou D. A review on the visible light active titanium dioxide photocatalysts for environmental applications. *Applied Catalysis B: Environmental* **2012**, 125, 331-349. <https://doi.org/10.1016/j.apcatb.2012.05.036>

Quyen V.T., Jitae K., Huong P.T., Ha L.T.T., Than D.M., Viet N.M., Thang P.Q. Copper doped titanium dioxide as a low-cost visible light photocatalyst for water splitting. *Solar Energy* **2021**, 218, 150-156. <https://doi.org/10.1016/j.solener.2021.02.036>

Rahimi N., Pax R.A., Gray M.A. Review of functional titanium oxides. I: TiO₂ and its modifications. *Progress in Solid State Chemistry* **2016**, 44, 86-105. <https://doi.org/10.1016/j.progsolidstchem.2016.07.002>

Serin N., Serin T., Horzum H., Çelik Y. Annealing effects on the properties of copper oxide thin films prepared by chemical deposition. *Semiconductor Science and Technology* **2005**, 20, 398. <https://iopscience.iop.org/article/10.1088/0268-1242/20/5/012>

Sohrabi S., Akhlaghian F. Modeling and optimization of phenol degradation over copper-doped titanium dioxide photocatalyst using response surface methodology. *Process Safety and Environmental Protection* **2016**, 99, 120-128. <https://doi.org/10.1016/j.psep.2015.10.016>

Spurr R.A., Myers H. Quantitative analysis of anatase-rutile mixtures with an X-ray diffractometer. *Analytical Chemistry* **1957**, 29, 760-762. <http://dx.doi.org/10.1021/ac60125a006>

Thamaphat K., Kaewwiset W., Limsuwan P. Application of ESR Technique to Distinguish the Phase and Size of TiO₂ Powders *Journal of Electronic Science and Technology* **2010**, 8, 31-34. doi: 10.3969/j.issn.1674-862X.2010.01.006

Thambiliyagodage C.; Mirihana S. Photocatalytic activity of Fe and Cu co-doped TiO₂ nanoparticles under visible light. *Journal of Sol-Gel Science and Technology* **2021**, 99, 109-121. <https://doi.org/10.1007/s10971-021-05556-4>

Ullattil S.G., Periyat P. (2017). Sol-Gel Synthesis of Titanium Dioxide. In: Pillai, S., Hehir, S. (eds) Sol-Gel Materials for Energy, Environment and Electronic Applications. Advances in Sol-Gel Derived Materials and Technologies. Springer, Cham. https://doi.org/10.1007/978-3-319-50144-4_9

Yoong, L. S.; Chong, F. K.; Dutta, B. K. Development of copper-doped TiO₂ photocatalyst for hydrogen production under visible light. *Energy* **2009**, 34, 1652-1661. <https://doi.org/10.1016/j.energy.2009.07.024>

Zhang S., Ma H., Ya L., Cao W., Yan T., Wei Q., Du B. Copper-doped titanium dioxide nanoparticles as dual-functional labels for fabrication of electrochemical immunosensors. *Biosensors and Bioelectronics* **2014**, 59, 335-341. <https://doi.org/10.1016/j.bios.2014.03.060>

Zhang X., Chen Y., Shang Q., Guo Y. Copper doping and organic sensitization enhance photocatalytic activity of titanium dioxide: Efficient degradation of phenol and tetrabromobisphenol A. *Science of The Total Environment* **2020**, 716, 137144. <https://doi.org/10.1016/j.scitotenv.2020.137144>

Zhou W., Wang Z.L. (2007) Scanning Microscopy for Nanotechnology. Techniques and Applications. SpringerLink. <https://doi.org/10.1007/978-0-387-39620-0>

TERMS AND ABBREVIATIONS

AFM - Atomic force microscopy

BET - Brunauer-Emmet-Teller theory

Cu - Copper

CuO - Copper (II) oxide

Cu + Ti - Product where the copper was added first in synthesis, then the titanium

d - Interplanar distance between x-ray planes in XRD

DRS - Diffuse reflectance spectroscopy

EIS - Electrochemical impedance spectroscopy

Fe - Iron

Fe₃O₄ - Iron (II, III) oxide black magnetite

Fe + M - Product where the iron was added first in synthesis, then the titanium

M + Ti - Product where the copper and iron was added first in synthesis, then the titanium

SEM - Scanning electron microscopy

TEM - Transmission electron microscopy

Ti - Titanium

TiO₂ - Titanium dioxide

Ti + Cu - Product where the titanium was added first in synthesis, then the copper

Ti + Fe - Product where the titanium was added first in synthesis, then the iron

Ti + M - Product where the titanium was added first in synthesis, then the copper and iron

UV-Vis - UV-visible spectroscopy

XPS - X-ray photoelectron spectroscopy

XRD - X-ray diffraction

XRF - X-ray fluorescence

APPENDIX

Appendix 1. Reference data for XRD

Table S.1. Reference XRD patterns for Anatase and Rutile

Rutile (JCPDS no.: 88-1175)		Anatase (JCPDS no.: 84-1286)	
2 θ (°)	Relative height	2 θ (°)	Relative height
27.70	100	25.20	100
36.40	46	37.00	7
39.80	7	37.90	19
41.80	16	38.50	7
44.80	6	48.00	26
55.00	50	53.90	16
57.50	12	55.20	16
63.00	6	62.80	12
65.20	6	68.80	5
70.00	16	70.20	5
70.20	9		

Appendix 2. Example of calculation of crystallinity parameters

Grain Size

Calculation of grain size from XRD data. Reference: Nanoworld videos Crystallites (grain) size from XRD data using Scherrer equation - 09 - YouTube

Step 1. Calculate the half width at full max.

Manually: Normalized the peak by dividing each Y value of by the maximum Y value of the peak. In this way, the maximum height becomes 1. Identify the two X values where Y is 0.5. Subtract the two X values to get the width of the peak.

Alternatively, use Origin or excel template for all the peaks. [How to find peak position and FWHM of XRD data - 08 - YouTube](#)

Step 2. Calculate θ by dividing the position of the maximum by 2.

Step 3. Calculate crystallite size using use the Scherrer equation

$$\Phi = \frac{K \lambda}{\beta \cos \theta}$$

where Φ is the crystallite size, K is the shape factor (0.9 is typically used), λ is the X-ray wavelength (0.15406 nm), β is the FWHM and θ is the Bragg angle. Use radians for angle values (β and θ).

Step 4. Calculate average and standard deviation.

Table S.2. Example of values used to calculate crystallite size for TiO₂ sample. FWHM was calculated in origin. Average size = 21 ± 1 nm

2θ	θ	FWHM	Crystallite Size (nm)
25.35	12.68	0.38343	21.23671
37.85	18.93	0.39109	21.47402
48.15	24.08	0.38564	22.56327
53.98	26.99	0.44157	20.18966
55.18	27.59	0.41666	21.51256
62.77	31.38	0.49679	18.73182
68.85	34.42	0.42309	22.76338
70.41	35.20	0.41228	23.58247
75.15	37.58	0.46876	21.38361

Lattice parameters

Lattice parameters calculated using XRD data. Reference: How to calculate lattice constant (a, b, c) values of a unit cell from XRD data -12- YouTube.

Step 1. Determine the 2θ that relates to Millar indices (h, k, l) 200 and 101.

Step 2. Calculate the interplanar distance (d) for both angles with the equation below:

$$d = \frac{n\lambda}{2\sin\theta}$$

Where n is 1, λ is the X-ray wavelength (0.15406 nm), and θ is the angles from step 1 divided by 2. Use θ in radians.

Step 3. Calculate parameter a with the tetragonal Bragg's equation using the peak with Millar indices 200:

$$\frac{1}{d^2} = \frac{h^2}{a^2} + \frac{k^2}{b^2} + \frac{l^2}{c^2}$$

Where d is the interplanar distance for Millar indices 200, h is 2, k is 0, l is 0. This allow parameters b and c to be ignored and a can be solved for with the following equation:

$$a = hd$$

Since the crystal is tetragonal, lattice parameters a and b are equal, hence b does not need to be calculated.

Step 4. Calculate parameter c with the tetragonal Bragg's equation with Millar indices 101.

$$\frac{1}{d^2} = \frac{h^2}{a^2} + \frac{k^2}{b^2} + \frac{l^2}{c^2}$$

Where d is the interplanar distance for Millar indices 101, h is 1, k is 0, l is 1, and a is the calculated value from step 3. This causes the parameter for b to be ignored and c can be solved for with the following equation:

$$c = \left(\frac{1}{d^2} - \frac{1}{a^2} \right)^{-0.5}$$

Appendix 3. Calculation of Anatase and Rutile proportions from XRD data

The fraction of rutile was calculated using the Spurr equation. [Spurr 1957].

$$F_R = \left(1 + 0.8 \left[\frac{I_{A(101)}}{I_{R(110)}} \right] \right)^{-1}$$

where $I_{A(101)}$ and $I_{R(110)}$ are the intensities of the main diffraction peaks of anatase and rutile.

Percent was obtained by multiplying the fraction by 100.

Table S.3. Summary of maximum intensity of the main diffraction peak

Sample	Main diffraction peak (°)		Intensity	
	Anatase (101)	Rutile (110)	Anatase (101)	Rutile (110)
TiO ₂	25.4	27.5	71791	1175
Roasted reagents	25.4		75885	
Ti+M	26.0	28.1	2326	1989
M+Ti	25.8	27.9	2844	5249
Ti +Fe	25.6		6140	
Ti + Cu	25.7		7207	
Fe+ Ti	25.8		5964	
Cu+ Ti	26.1		5696	

Table S.4. percent of anatase and rutile for sample that showed both diffraction patterns

Sample	% Anatase (101)	%Rutile (110)
TiO ₂	98	2
Ti+M	48	52
M+Ti	30	70

Appendix 4. Calculation of band gap from DRS Kubelka-Munk function and Tauc plot method

In DRS the band gap of a semiconductor corresponds to the energy (E) in which the ratio of absorption and scattering (F(R)) shifts. In a graph of F(R) vs E, the band gap energy is obtained by extrapolating F(R) to zero at the point of shift. Using proper approximation [Landi 2022], the graph should be $(F(R) \times E)^{1/2}$ vs E.

Step 1. Convert wavelength into energy using the relation $E = \frac{hc}{\lambda}$

where Plank's constant is $h = 4.13 \times 10^{-15}$ eV and speed of light is $c = 3.0 \times 10^{17}$ nm/s.

Step 2. Calculate the function F(R) as the absorption over scattering; this is $F = \frac{(1-R)^2}{2R}$

where R is the refraction measured in DRS.

Step 3. Plot $(F(R) \times E)^{1/2}$ vs E and do a linear regression of the vertical change to get the equation:

$$(F(R) \times E)^{1/2} = (\text{Slope} \pm \Delta\text{Slope}) * E + (\text{Intercept} \pm \Delta\text{Intercept})$$

Obtain the errors using LINEST in excel.

Step 4. Calculate the band gap energy (E_g) by extrapolating the Y-axis to zero

$$E_g = \frac{-\text{Intercept}}{\text{Slope}}$$

Step 5. Calculate the error by propagation

$$\Delta E_g = E_g \sqrt{\left(\frac{\Delta\text{Intercept}}{\text{Intercept}}\right)^2 + \left(\frac{\Delta\text{Slope}}{\text{Slope}}\right)^2}$$

Appendix 5. XRF data

Table S.6. Intensity at titanium, iron, copper, and sum titanium K energy levels for the titanium dioxide control, roasted reagents, and co-doped products.

Element energy level	Energy (keV)	Intensity calcined reagents	Intensity TiO ₂	Intensity Ti + M	Intensity M + Ti
Ti K_{α1}	4.499	502,690	646,704	653,016	649,314
Ti K_{β1}	4.921	78,987	101,249	102,604	102,018
Fe K_{α1}	6.407	35,291	1,382	1,651	1,642
Fe K_{β1}	7.070	6,533	863	990	959
Cu K_{α1}	8.034	95,191	1,432	1,994	1,905
Cu K_{β1}	8.918	16,845	2,966	3,382	3,267
Ti K_{α1}+Ti K_{α1}	9.038	8,053	7,356	7,044	7,010
Ti K_{α1}+Ti K_{β1}	9.460	2,158	2,842	2,756	2,705

Table S.7. Intensity at titanium, iron, copper, and sum titanium K energy levels for copper and iron doped products.

Element energy level	Energy (keV)	Intensity Ti + Cu	Intensity Cu + Ti	Intensity Ti + Fe	Intensity Fe + Ti
Ti K_{α1}	4.499	628,877	629,433	635,142	639,393
Ti K_{β1}	4.921	98,004	99,236	99,299	100,072
Fe K_{α1}	6.407	1,360	1,360	1,632	1,536
Fe K_{β1}	7.070	956	903	970	932
Cu K_{α1}	8.034	1,949	1,949	1,371	1,362
Cu K_{β1}	8.918	2,569	2,836	2,709	2,695
Ti K_{α1}+Ti K_{α1}	9.038	7,315	6,739	7,172	7,180
Ti K_{α1}+Ti K_{β1}	9.460	2,705	2,691	2,705	2,776

Appendix 6. Proportion of Fe:Cu in co-doped products

The roasted reagents contained 0.015 mol CuO, which corresponds to 0.015 mol of copper, and 0.005 mol Fe₃O₄, which corresponds to 0.015 mol of iron.

In the roasted reagents, the XRF intensity of copper was 95191 and iron was 35291.

Considering a response factor R for each element, we can write that the XRF response (I) is

$$I_{Cu} = R_{Cu} * \text{amount of copper}$$

$$I_{Fe} = R_{Fe} * \text{amount of iron}$$

Thus
$$\frac{R_{Cu}}{R_{Fe}} = \frac{I_{Cu} * \text{mol of iron}}{I_{Fe} * \text{mol of copper}} = \frac{95191 * 0.015 \text{ mol iron}}{35291 * 0.015 \text{ mol copper}} = 2.7$$

This indicates that from equalmolar amount, the signal of copper is 2.7 times larger than that of iron.

To calculate the relative mole amounts of copper and iron in the products, consider

$$\frac{\text{mol iron}}{\text{mol copper}} = \frac{I_{Fe} * R_{Cu}}{I_{Cu} * R_{Fe}} = \frac{I_{Fe}}{I_{Cu}} * 2.7$$

In the Ti + M co-doped product the XRF intensity of copper was 1994 and iron was 1651.

Thus, in Ti + M co-doped product
$$\frac{\text{mol iron}}{\text{mol copper}} = \frac{1651}{1994} * 2.7 = 2.2$$

In the Ti + M co-doped product the XRF intensity of copper was 1905 and iron was 1642.

Thus, in M + Ti co-doped product
$$\frac{\text{mol iron}}{\text{mol copper}} = \frac{1642}{1905} * 2.7 = 2.3$$